# Power-Efficient Design Techniques for mm-Wave Hybrid/Digital FDD/Full-Duplex MIMO Transceivers

Susnata Mondal<sup>®</sup>, Student Member, IEEE, and Jeyanandh Paramesh<sup>®</sup>, Senior Member, IEEE

Abstract—This article describes system and circuit design techniques to enhance power efficiency and incorporate new features in millimeter-wave multi-input-multi-output (MIMO) transceivers. The higher peak-to-average power ratio (PAPR) of the signal transmitted from a digital beamformer (DBF) or a fully connected hybrid beamforming (FC-HBF) transmitter compared with the conventional partially connected hybrid beamforming (PC-HBF) transmitter is identified for the first time. It is then shown that when a power amplifier (PA) with better back-off efficiency than Class-A PA is used, the overall power efficiency of the FC-HBF is superior to the PC-HBF for a given antenna geometry. Second, a new mechanism for built-in dual-band, per-element self-interference cancellation (SIC) is introduced to enable multi-antenna frequency-division-duplex (FDD) and fullduplex (FD) operation. Such SIC can only be supported in the proposed FC-HBF architecture. Several innovative circuit concepts are introduced, including low-loss wideband antenna interface design, dual-band power combining PA, dual-band RF-SIC design, and bidirectional MIMO signal path design. To demonstrate these techniques, a 28-/37-/39-GHz bidirectional two-stream front-end single-element prototype is designed in the 65-nm CMOS. The prototype can be configured as a transmit (TX) or receive (RX) element in DBFs or FC-HBFs which can in turn be configured to support TDD, FDD, or FD operation. The front-end achieves 16-/11-dB RX gain, 6.2-/7-dB NF, 15.8-/16.8-dBm saturated PA output power, and 20%/21.6% peak PA efficiency in the 28-/37-GHz bands. Extensive characterization results are presented to compare the energy efficiencies of the PC-HBF and FC-HBF architectures. The prototype is also characterized in the FDD/FD mode and achieves 36-dB peak RF-domain SIC and better than 26-dB RF-domain SIC across 0.5-GHz modulation bandwidth.

Index Terms—Carrier aggregation (CA), digital beamforming, fifth-generation (5G), full-duplex (FD), fully connected (FC), hybrid beamforming, millimeter-wave transceiver, multi-input-multi-output (MIMO), self-interference cancellation (SIC), simultaneous transmit and receive (STAR).

#### I. INTRODUCTION

ILLIMETER (mm)-wave communication based on beamforming and multi-input-multi-output (MIMO) techniques is expected to be a revolutionary new element in

Manuscript received October 19, 2019; revised January 10, 2020 and March 14, 2020; accepted March 29, 2020. This article was approved by Guest Editor Payam Heydari. This work was supported in part by the National Science Foundation under Grant ECCS-1343324, Grant CCF-1314876, and Grant CRI-1823235. (Corresponding author: Susnata Mondal.)

The authors are with the Department of Electrical and Computer Engineering, Carnegie Mellon University, Pittsburgh, PA 15213 USA (e-mail: susnatam@andrew.cmu.edu; paramesh@ece.cmu.edu).

Color versions of one or more of the figures in this article are available online at http://ieeexplore.ieee.org.

Digital Object Identifier 10.1109/JSSC.2020.2987691

fifth-generation (5G) and beyond-5G wireless networks. Many single-band RF beamforming systems (i.e., phased arrays) have been demonstrated [1]-[7], which support single-stream communication in a single mm-wave band. Multi-element multi-stream mm-wave MIMO over a single band was first reported in the receiver of [8]1. Here, we demonstrated the so-called fully connected (FC) hybrid beamforming (HBF) architecture and showed its superior energy efficiency compared with the partially connected (PC) HBF receiver, which uses a conventional phased array for each stream. In [9], we demonstrated an efficient architecture and associated circuit implementation for reconfigurable, dual-band FC hybrid MIMO/beamforming reception. Here, image-rejection heterodyne downconversion was used in conjunction with Cartesian-combining-based beamforming [10] to demonstrate dual-band MIMO/beamforming in the 28- and 37-40-GHz bands. In addition to supporting MIMO in each band, the dualband FC-HBF receiver architecture in [9] also supported an efficient inter-band multi-antenna carrier aggregation (CA) mode where each aggregated carrier could access the full antenna aperture, and hence achieved full beamforming gain in each band. In [9], we also showed how adaptive beamforming can be implemented within a hardware constrained hybrid beamformer. Here, optimal minimum-mean-square-error beam/null-steering was demonstrated in hardware. In [11], a "partially overlapped" HBF topology, which lies between the FC and the PC HBF topologies, was reported. Jeon et al. [12] report a multi-beam local oscillator (LO)-shifting/IFcombining phased-array receiver. Multi-stream beamforming at IF has been reported in the receiver designs of [13]–[15].

This article, which expands upon [16], presents two innovative system concepts for beyond-5G multi-antenna systems. First, the increase in the peak-to-average power ratio (PAPR) in an FC-HBF [see Fig. 1(b)] transmitter compared with a PC-HBF [see Fig. 1(a)] is identified for the first time. It is shown that digital beamformers (DBFs) have the same PAPR considerations as the FC-HBF for an equivalent number of streams. The energy efficiencies of the FC-HBF and PC-HBF transmitters are then compared analytically and experimentally for modulated signals. It is shown that to

<sup>1</sup>A related work that is functionally similar to [8] is the two-element multibeam receiver front-end in [45], which demonstrated independent complex-valued weighting of the signals from two antennas to four outputs; however, its potential applicability to multi-stream MIMO operation was not noted or characterized in [45], nor did the prototype incorporate downconversion or local oscillator (LO) distribution.

0018-9200 © 2020 IEEE. Personal use is permitted, but republication/redistribution requires IEEE permission. See https://www.ieee.org/publications/rights/index.html for more information.

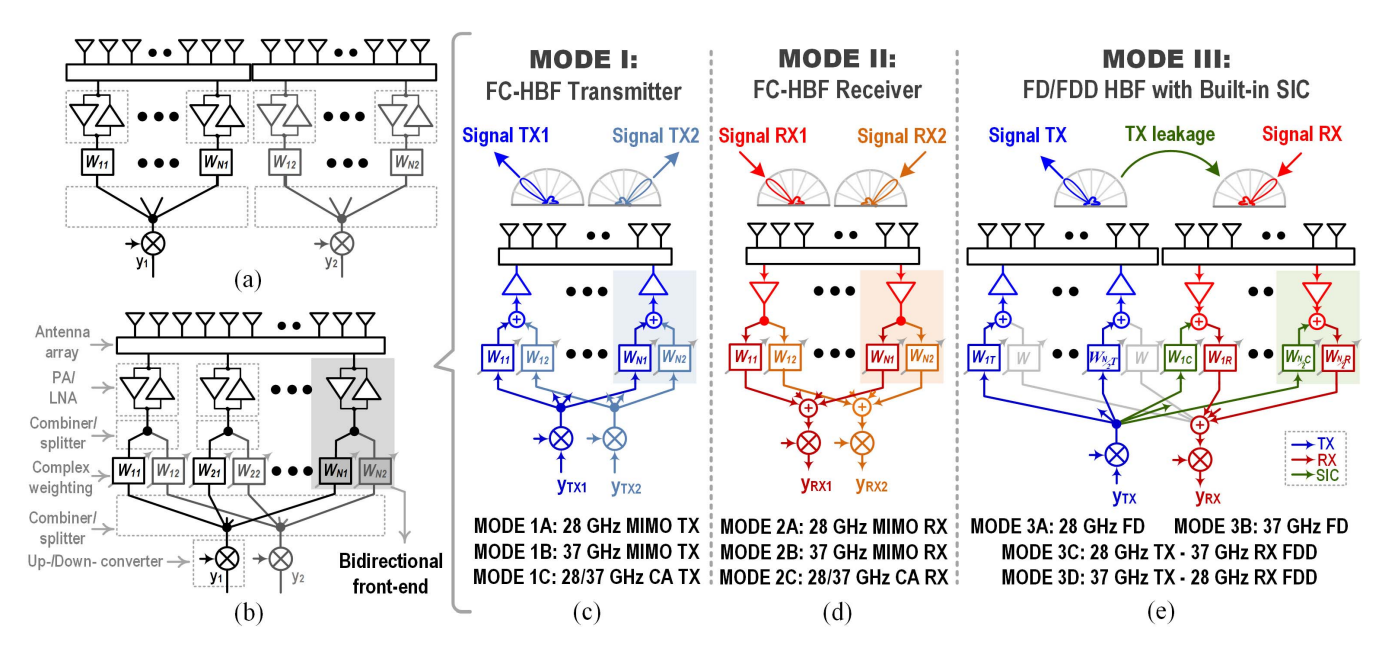


Fig. 1. (a) Partially connected HBF transceiver. (b) FC HBF transceiver. (c) FC-HBF transmit mode. (d) FC-HBF receive mode. (e) FDD/FD beamforming mode built-in SIC.

achieve identical spectral efficiency, the FC-HBF consumes significantly lower power than the PC-HBF when any power amplifier (PA) topology that has a better back-off efficiency characteristic than Class-A is used. Second, a new architecture is conceived which directly enables simultaneous transmit and receive (STAR) beamforming for multi-antenna frequency-division-duplex (FDD) or full-duplex (FD) communication. Our FC-HBF structure can be reconfigured to enable self-interference cancellation (SIC) on a per-element basis without hardware overhead. Such SIC is not possible in a PC-HBF.

To demonstrate the aforementioned system concepts, a compact circuit implementation is introduced. The circuit architecture can support bidirectional transmit or receive operation at 28 GHz, 37/39 GHz, or concurrently in both bands. Reconfiguration between multiple bands helps avoid the use of a dedicated beamforming module for each band, thereby reducing overall system complexity, area, and cost. Three main configuration modes and ten sub-modes are available. Mode I [see Fig. 1(c)] and Mode II [see Fig. 1(d)] are time-division-duplexed (TDD) FC-HBF transmit and receive modes, respectively. Modes I and II can be configured for multi-stream MIMO operation in each band (in sub-modes A and B) or inter-band CA (in sub-mode C). Mode III [see Fig. 1(e)] enables FDD/FD, where half of the array is configured as TX and another half as RX with built-in SIC.

A 28-/37-/39-GHz bidirectional two-stream front-end prototype has been designed. Passive elements are extensively reused in the TX and RX modes to reduce the die area. The front-end features several new circuit techniques including 1) a multi-band, low-loss interface network between the antenna port, the low-noise amplifier (LNA), and the PA; 2) power-combining Class-B PA with a dual-band second-harmonic shorting network; 3) self-neutralized bidirectional programmable-gain amplifier (PGA); 4) reconfigurable combiner/splitter to support incorporation into the

FC-HBF transceivers; and 5) dual-band RF self-interference (SI) canceller.

# II. ENERGY EFFICIENCY OF FULLY CONNECTED VERSUS PARTIALLY CONNECTED HBF TRANSMITTER

Several articles in the system literature have noted that HBFs can support multi-stream MIMO communication with superior energy efficiency than DBF [8], [9], [17]-[21]. In [8], we showed that between the two types of HBF receivers, the FC-HBF RX achieves superior spectral and energy efficiency than the PC-HBF RX for a given antenna geometry. The FC-HBF receiver can also synthesize narrower beams resulting in better spatial filtering. The energy efficiency of systems using the FC- and PC-HBF TX has been compared in the systems' literature [18]-[21]. However, it has not been previously appreciated that the output signal power characteristics for the two architectures are very different. This, in turn, greatly affects the PA power consumption, which is the most significant source of power consumption in the transmitter array. In this section, we compare the FC- and PC-HBF transmitters taking this issue into account.

# A. Advantages and Disadvantages of FC-HBF Transmitter

1) Lower Average Output Power Specification: The equivalent isotropically radiated power (EIRP) of a multi-antenna transmitter scales quadratically with the number of antennas due to coherent spatial combining. In a PC-HBF [see Fig. 1(a)] TX, each stream accesses  $N_T/N_S$  antennas where  $N_T$  and  $N_S$  are the total number of antennas and streams, respectively. Hence, as shown in Table I, to radiate per-stream EIRP of  $P_{\rm rad}$ , the average output power specification of each PA in a PC-HBF TX is  $P_{\rm rad} \times (N_S/N_T)^2$ . On the other hand, in an FC-HBF [see Fig. 1(b)] all  $N_S$  streams access all  $N_T$  antennas, and hence, to radiate the same per-stream EIRP

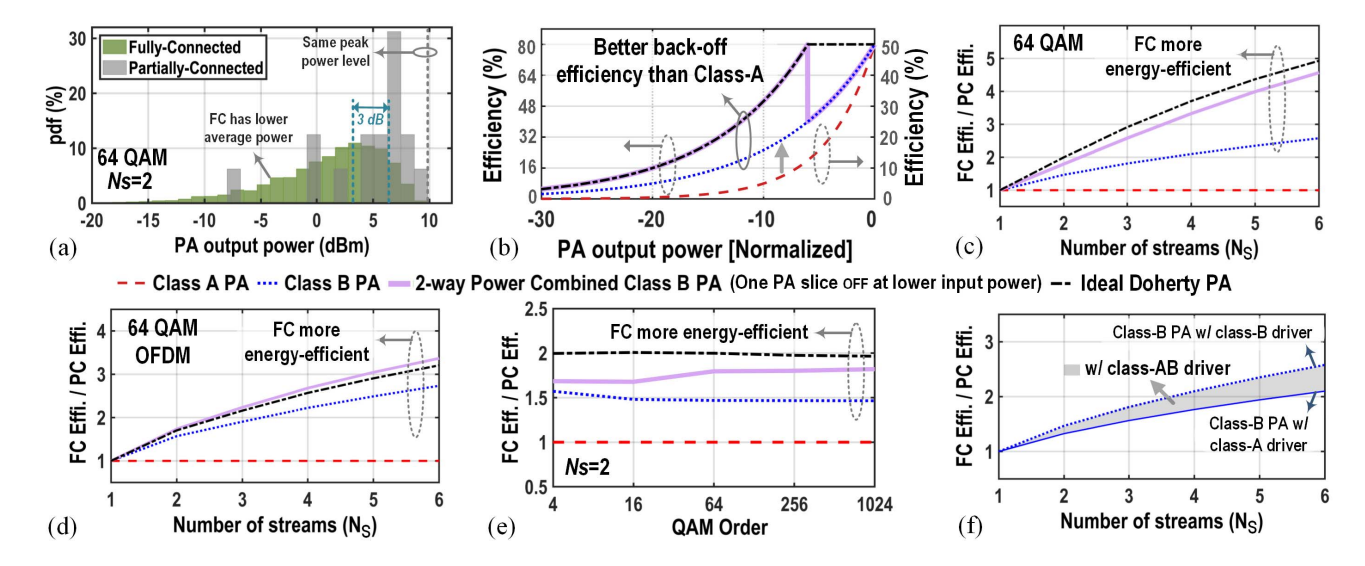


Fig. 2. (a) PA output power distribution of FC- and PC-HBF TX ( $N_S = 2$ ) for the 64-QAM modulation scheme showing the increase in PAPR in the FC case. (b) Back-off characteristics of four different ideal PA topologies used in simulation to compare the FC and PC cases. PA energy efficiency improvement in FC-HBF with respect to PC-HBF (c) versus  $N_S$  for the 64-QAM modulation scheme, (d) versus  $N_S$  for the 64-QAM oFDM modulation scheme, and (e) versus QAM modulation order for  $N_S = 2$ . (f) PA energy efficiency improvement in FC-HBF with respect to PC-HBF for Class-B output stage and Class-AB driver stage.

 $P_{\rm rad}$ , each PA needs to transmit the average power of only  $N_S \times P_{\rm rad} \times (I/N_T)^2$ . Therefore, for identical antenna geometry, the FC-HBF TX achieves identical link budget or spectral efficiency as the PC-HBF TX while transmitting  $I/N_S$  times lower average output power per PA.

- 2) Identical Peak Output Power Specification: In a FC-HBF TX, independent signals from all  $N_S$  streams are combined before transmission. This can be conveniently done at each PA. However, this increases the PAPR of each PA's input signal by  $N_S$  times over the raw modulation-dependent PAPR of the PA's input in a PC-HBF TX. Therefore, as shown in Table I, because the FC-HBF TX has  $I/N_S$  times the average output power, but  $N_S$  times the PAPR, the PAs in the FC-HBF TX and the PC-HBF TX have identical peak output power specification.
- 3) Lower DC Power Consumption: Next, consider FC-HBF and PC-HBF transmitters where both use hypothetical PAs having constant back-off efficiency. Because the FC-HBF transmits  $I/N_S$  times lower average output power, it would also consume  $I/N_S$  times lower DC power in each PA but would achieve identical spectral efficiency to the PC-HBF. This is a tremendous advantage of the FC-HBF over the PC-HBF. However, this margin of superiority decreases with the use of real PA topologies. In the case of a Class-A PA, as the power consumption at back-off is the same as at the peak, the PAs in both the PC-HBF and the FC-HBF transmitters would consume identical DC power. However, for other PA topologies that have better back-off efficiency than Class-A, the FC-HBF would consume less DC power than the PC-HBF.

# B. Considerations for DBF

The PAs in a DBF have identical specifications to an FC-HBF for the same  $N_T$  and  $N_S$ . Therefore, if a Class-A

TABLE I FC VERSUS PC HBF PA

	PC	FC								
EIRP per stream	$P_{rad}$									
No. of streams	$N_s$									
No. of antennas	$N_{PC} = N_T$	$N_{FC} = N_T$								
Average output power of PA	$\begin{split} &P_{rf-av-PC} \bigg(\frac{N_T}{N_S}\bigg)^2 = P_{rad} \\ &\Rightarrow P_{rf-av-PC} = P_{rad} \bigg(\frac{N_S}{N_T}\bigg)^2 \end{split}$	$\begin{aligned} &P_{rf-av-FC} \left( N_T \right)^2 = P_{rad} \times N_S \\ &\Rightarrow P_{rf-av-FC} = P_{rad} \left( \frac{N_S}{N_T^2} \right) \end{aligned}$								
Conclusion #1:	PA's in FC need less	average output power								

PAPR	$PAPR_{MOD}$	$PAPR_{MOD} \times N_{S}$						
Peak output power of PA	$\begin{aligned} & P_{rf-pk-PC} \\ & = P_{rf-av-PC} \times PAPR_{MOD} \\ & = P_{rad} \left( \frac{N_S}{N_T} \right)^2 \times PAPR_{MOD} \end{aligned}$	$\begin{split} & P_{rf-pk-FC} \\ & = P_{rf-av-FC} \times PAPR_{MOD} \times N_S \\ & = P_{rad} \left( \frac{N_S}{N_T} \right)^2 \times PAPR_{MOD} \end{split}$						

**Conclusion #2:** PA's in FC and PC have equal output power requirements

PA topology is chosen, the PAs in DBF would consume identical DC power to PC-HBF to achieve the same spectral efficiency. Considering that the TX components other than the PAs in a DBF consume more power than PC-HBF, DBF TX with Class-A PA is always less energy-efficient than PC-HBF TX. However, if a PA topology with good back-off efficiency is chosen, the PAs in a DBF can provide significant power saving over PC-HBF, potentially achieving better overall TX efficiency than PC-HBF.

#### C. System Simulation Results

Fig. 2(a) shows a system simulation of the PA output power distribution of FC- and PC-HBFs with  $N_S = 2$  and 64-QAM

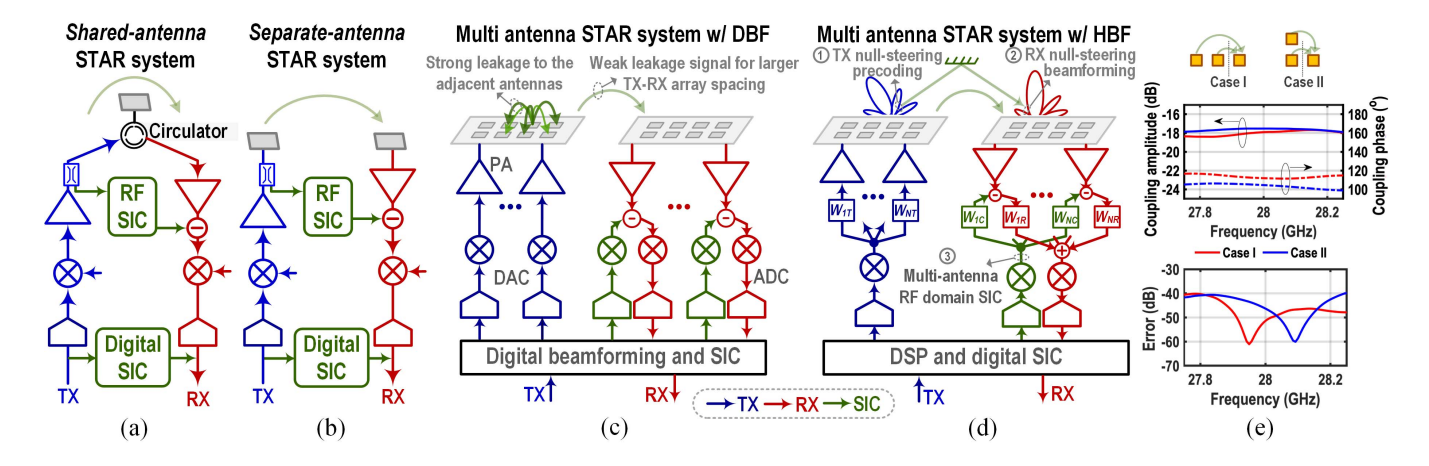


Fig. 3. (a) Shared-antenna STAR system. (b) Separate-antenna STAR system. (c) Multi-antenna STAR systems with DBF and analog domain SIC. (d) Multi-antenna STAR system with FC-HBF featuring per-element SIC. (e) Antenna coupling amplitude and phase variation, and resulting single tap estimation error across frequency for two different antenna coupling scenarios.

modulation. It can be seen that the FC-HBF and the PC-HBF have identical peak power requirements and that the FC-HBF has higher PAPR (hence lower average output power). The next simulation quantifies the superiority of FC-HBF over PC-HBF for four common PA topologies, whose theoretical back-off efficiency characteristics are shown in Fig. 2(b). The following conclusions can be drawn from Fig. 2(c): 1) Class-A PA results in identical system efficiency; 2) any PA with better back-off efficiency than Class-A results in greater system efficiency improvement for the FC; and 3) the superiority of FC improves with  $N_S$ . The energy efficiency improvement in FC-HBF PAs is shown across  $N_S$  for 64-QAM in Fig. 2(c), for 64-QAM-OFDM in Fig. 2(d), and for  $N_S = 2$  versus QAM order in Fig. 2(e). These results show that energy efficiency superiority of the FC-HBF holds for a wide variety of modulation schemes. Fig. 2(f) shows the PA efficiency improvement in FC-HBF versus  $N_S$  for a PA having a Class-B output stage and a driver stage biased at different levels between Class-A and Class-B. The efficiency improvement can be seen to remain nearly the same for a Class-B driver stage and drops slightly for a Class-AB driver stage [denoted by the gray shaded region in Fig. 2(f)].

# III. SIMULTANEOUS TRANSMIT AND RECEIVE BEAMFORMING

STAR operation in separate transmit/receive frequency channels is equivalent to FDD. STAR operation in a single channel is called FD and results in doubling in throughput (a theoretical maximum) compared to a TDD system. In both FDD and FD, a key challenge is the SI due to the strong transmit signal that can leak into the path of the weak received signal resulting in severe corruption through interference and non-linearity. In the case of FDD, the leakage can be partially attenuated by filtering in the front-end diplexer. However, this mechanism is not available in the FD case, and therefore, signal cancellation of the transmit signal leakage is the only viable option.

There are two variants of STAR systems: shared-antenna STAR [see Fig. 3(a)] [22], [23], where each antenna element

is shared between the transmit and receive paths, and separateantenna STAR [see Fig. 3(b)] [24], [25], where the transmit and receive paths use separate antennas. While the sharedantenna approach has gained interest in sub-6-GHz STAR communication [22], [23], the separate-antenna approach is advantageous in a mm-wave multi-antenna beamforming system for the following reasons.

- 1) The separate-antenna approach avoids the use of a circulator. Recent innovations have made on-chip implementation of circulators possible [23], [26], [27], but they are lossy, have limited linearity and bandwidth, and achieve inadequate transmit-receive isolation. Furthermore, they occupy large die area and are difficult to integrate into multi-antenna transceivers with large numbers of elements in a cost-effective manner.
- 2) More importantly, due to small element spacing at mm-wave, the adjacent elements experience significant coupling [28]; hence, inter-element SI between nearby elements would be severe in the shared-antenna approach. In a circulator-based STAR beamforming system, although the circulator in each element isolates the receiver from SI from its own transmit signal, SI from the adjacent elements pass through the circulator with little attenuation. However, in a separate-antenna approach, SI due to antenna coupling can be greatly reduced by increasing the physical spacing between the transmit and receive antenna arrays.

A single separate-antenna STAR transceiver [see Fig. 3(b)] can be extended to a multi-antenna transceiver as shown in Fig. 3(c). The transmit path has a digital to analog converter (DAC), upconverter, and PA in each element along with digital precoding, while the receive path has LNA, downconverter, and analog to digital converter (ADC) in each element along with digital beamforming. However, the conventional method of performing RF SIC by feeding a weighted PA signal to the canceller path [22], [24], [25] is impractical in a multi-antenna system because feedback from each TX antenna to every RX antenna would be required. Therefore, as shown in Fig. 3(c),

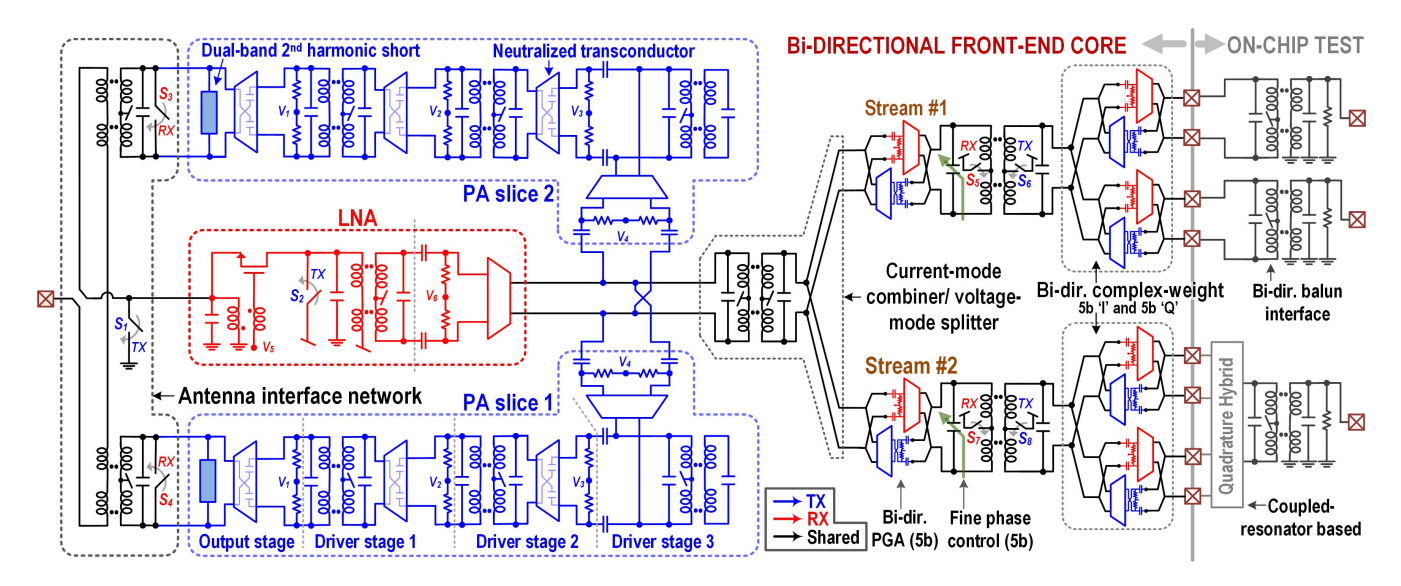


Fig. 4. Schematic of 28-/37-/39-GHz bidirectional TRX FC-HBF/DBF channel core and on-chip test circuitry. The TX path, the RX path, and the shared path are shown in blue, red, and black, respectively.

an RF domain cancellation signal must be generated separately for each element in the RX array using an upconverter and DAC per element to perform per-element SIC. The back-end digital processing can further reduce the SI by optimizing the TX leakage in the TX array and by canceling the residual SI in the digital domain in the RX array.

In Fig. 3(d), we show how the aforementioned SIC approach can be implemented in the proposed bidirectional FC-HBF [see Fig. 1(e)]. Here, a reduced number of bidirectional frequency translation chains (i.e., streams) interface to a large number of antennas through per-element bidirectional RF-domain complex weights. Two separate FC-HBF transceivers are used in the FD system, one each for TX and RX. In the TX FC-HBF, one stream is configured for transmit. In the RX FC-HBF, one stream is configured for receive, while the other stream is repurposed to upconvert a copy of the baseband transmit signal. The upconverted transmit signal copy can be independently complex weighted in each element to cancel the incoming transmit signal leakage, thereby performing a per-element SIC. Thanks to this built-in SIC mechanism, the FC-HBF transceiver offers an efficient basis for STAR beamforming without the need for additional cancellation circuitry. It is important to note that a similar SIC mechanism is not available in the PC-HBF.

In a multi-antenna STAR system, SI can occur in two ways: 1) through antenna coupling from the transmit to the receive antennas; 2) due to reflections of the transmitted signal into the receive antenna array. The first kind of SI has small group delay, while the second kind may have small or large group delays depending on the distance of the reflectors. Typically, the SI with lower group delay would be expected to have higher strength due to having lower path loss. While the DBF-based STAR system in Fig. 3(c) can cancel SI with both small and large group delays, the FC-HBF-based STAR system in Fig. 3(d) can only cancel the first kind of SI because only a single-tap cancellation can be independently applied in

each element. To show the usefulness of this SIC mechanism, the coupling between patch elements (same polarization) for two different multi-antenna configurations was measured. Over a 500 MHz signal bandwidth, the coupling has fairly flat amplitude and phase responses [see Fig. 3(e)], which can be estimated by a single tap (i.e.,  $\alpha e^{j\theta}$ ) with better than -40 dB estimation error. Moreover, in the FC-HBF, large group-delay SI can be canceled by directing a spatial null in the RX array toward the reflection paths in both the transmit and the receive beamformer (at the cost of some degradation of the main beam gain [28], [29]). Note that null-steering SIC cancels the SI only after beamforming, whereas the single-tap RF SIC cancels the SI right at the LNA output. Furthermore, note that nulls in both the TX and RX array patterns can be steered toward different leakage multipath components or toward the same path to achieve higher rejection.

#### IV. 28-/37-/39-GHz FC-HBF CIRCUIT DESIGN

To validate the aforementioned concepts, a reconfigurable, bidirectional, multi-band (28/37/39 GHz) FC-HBF transceiver front-end was designed in a 65-nm CMOS technology. A detailed schematic of the front-end is shown in Fig. 4. The prototype comprises a TX path (Fig. 4, blue parts) dual-band two-way power combining PA and an RX path (Fig. 4, red parts) LNA, both of which are interfaced to the antenna port using a shared multi-band antenna interface network (AIN; Fig. 4, black parts). Opposite to the antenna port, the LNA output and the PA input are interfaced with two bidirectional T/R streams, where each stream consists of a complex weight, a fine gain control, and a fine phase control. All large-area passive structures, except those inside the LNA and the PA, are shared in the TX and the RX paths for compactness. Moreover, all the signal path reconfigurations are done without using any switches in the signal path. Two sets of bidirectional PGAs are available for two-stream complex-weighting in

hybrid MIMO/beamforming. The bidirectional front-end can be used as the core building block of a multi-mode two-stream FC-HBF transceiver of the type shown in Fig. 1(b)–(e). This can be done in one of two ways: 1) by having one quadrature hybrid per element and per stream after the PGAs, followed by one parallel combiner for each stream or 2) using the dual-band Cartesian-combining approach similar to [9]. Also, note that by excluding the complex weights, the front-end can be used directly in a DBF [see Fig. 3(c)].

In the prototype, different off-chip interfaces are used for the weights in each stream; this is done solely for test purposes. In stream #1, the I-path and Q-path PGA's are connected via baluns to separate pads for standalone testing. In stream #2, a coupled-resonator-based quadrature hybrid [30] is used to implement full complex-weighting.

#### A. Multi-Band AIN

In this section, we consider the problem of designing a compact, multi-band AIN. We start by considering a common single-band solution where the antenna interface switch is implemented using a series quarter-wavelength ( $\lambda/4$ ) transmission line and a shunt switch, as shown in Fig. 5(a). On-chip  $\lambda/4$  transmission lines have large footprint and high insertion loss even at mm-wave frequencies [1], which degrade the TX output power ( $P_{\text{out}}$ ) and RX noise figure (NF). Partial solutions to this problem are proposed in the single-band (28 GHz) phased arrays reported in [1] and [4], where  $\lambda/4$  line in the TX path is eliminated, thereby avoiding the TX output power penalty. However, several shortcomings remain. In [1], a  $\lambda/4$ line is still required in the RX path and has large footprint and high loss. In [4], high inductance in the RX path affects the LNA input matching bandwidth. In the RX mode of both designs, the RX input experiences an LC-tuned OFF-state TX load that presents high impedance at the antenna port only over a narrow bandwidth; this adversely affects the RX input match bandwidth. More importantly, in the TX mode, the OFF-state RX-side switch in Fig. 5(a) and [1] loads the TX via the  $\lambda/4$  line, causing reduced TX bandwidth and output power. This loss can be estimated as follows. For a transmission line with characteristic impedance  $Z_0$  and quarter wavelength at frequency  $f_C$  terminated in a switch with resistance  $R_{ON}$ , the input impedance can be written as

$$Z_{\text{OFF}}(f) = Z_0 \frac{R_{\text{ON}} + jZ_0 \tan\left(\frac{\pi}{2} \times \frac{f}{f_c}\right)}{Z_0 + jR_{\text{ON}} \tan\left(\frac{\pi}{2} \times \frac{f}{f_c}\right)}$$

$$\stackrel{R_{\text{ON}} \to 0}{\longrightarrow} jZ_0 \tan\left(\frac{\pi}{2} \times \frac{f}{f_c}\right). \tag{1}$$

It is seen that the impedance looking into the RX is high at  $f_C$ , but has low reactive values as the operating frequency deviates from  $f_C$ . If a PA is designed for the optimal output impedance of the antenna  $Z_0$  at  $f_C$ , it can be shown that the PA's maximum output power at a frequency f in the presence of the OFF-state RX side impedance is given by [31]

$$\frac{P_{\text{out}}(f)}{P_{\text{out}}(f_C)} = \left(1 - \frac{Z_0^2}{Z_{\text{OFF}}^2(f)}\right)^{1/2} = \left(1 - \cot^2\left(\frac{\pi}{2} \times \frac{f}{f_C}\right)\right)^{1/2}.$$
(2)

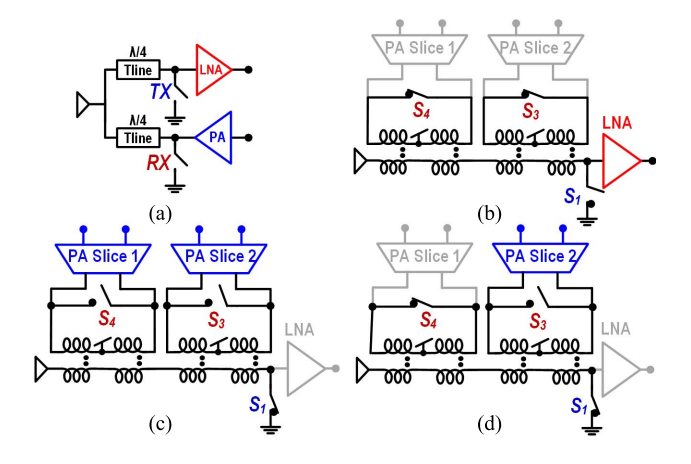


Fig. 5. (a) Conventional single-pole double-through switch without explicit series switches. Configuration of the proposed multi-band AIN in (b) RX mode, (c) HP TX mode, and (d) LP TX mode.

Thus, if a single-band design is used in the dual-band design at hand, the OFF-state RX-side impedance can cause as high as  $\sim$ 3 dB of loss at f=37 GHz for  $f_C=28$  GHz. Simulation conducted with the designed power combining PA shows similar output power degradation when a similar OFF-state switch is connected to the output of the PA.

Fig. 5(b)–(d) shows the various configuration modes of the proposed multi-band AIN, where an LNA and a two-way power combining PA are interfaced to an antenna port using a single passive network and three MOS switches S<sub>1</sub>, S<sub>3</sub>, and S<sub>4</sub>.

1) TX Mode: In the TX mode, LNA input switch  $S_1$  is in the ON-state. The AIN itself serves as the two-way power combining network. In the high-power (HP) TX mode [see Fig. 5(c)], switches  $S_3$  and  $S_4$  are both left open and both PA slices are turned ON. In the low-power (LP) TX mode, only  $S_3$  is open with one PA slice ON [see Fig. 5(d)]. This AIN design overcomes the bandwidth limitations of conventional front-end switches. It can be shown that the non-zero  $R_{\rm ON}$ of switch S<sub>1</sub> results in a loss of  $20 \times \log(1 + R_{ON}/50)$  dB, which is only  $\sim 0.3$  dB for  $R_{\rm ON} \sim 2$   $\Omega$ . A similar loss is estimated in simulation. Please note that although the LNA is turned OFF in the TX mode by turning off all the LNA biases, a non-negligible feedback signal still flows through the LNA from the PA's output to its input (see Fig. 4), which degrades PA stability. To further reduce the feedback signal strength, switch S<sub>2</sub> is turned ON (see Fig. 4), which significantly reduces the gain of the first LNA stage. 2) RX Mode: In the RX mode, LNA input switch S<sub>1</sub> is turned OFF, S<sub>3</sub> and S<sub>4</sub> are both turned ON, and both the PA slices are OFF, as shown in Fig. 5(b). Therefore, the RX path consists of a  $\pi$ -matching network with series inductance from AIN, the LNA input capacitance, and the antenna port capacitance. It can be shown that maximum series inductance  $L_{AIN}$  that can be used to match the LNA input impedance  $R_{i,LNA}$  to the antenna port input impedance of  $R_{i,ANT}$  at frequency f is given by

$$\max(L_{\text{AIN}}) = L_m = \sqrt{R_{i,\text{LNA}}R_{i,\text{ANT}}}/(2\pi f). \tag{3}$$

In the proposed design, turning ON the thick-gate NMOS switches S<sub>3</sub> and S<sub>4</sub> is especially advantageous. This is because,

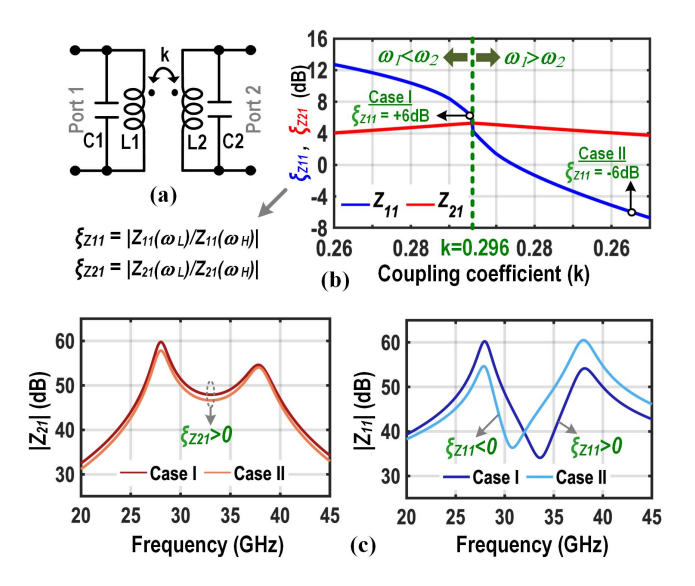


Fig. 6. (a) Schematic of transformer-coupled resonator load. (b) Ratio of the peak amplitudes in case of a dual-band  $Z_{11}$ - and  $Z_{21}$ -based coupled resonator load. (c)  $Z_{11}$  and  $Z_{21}$  frequency responses for two operating regions.

in the RX configuration, they help reduce the series inductance by a factor of  $(1-k^2)$  compared with when both switches are OFF. Therefore, by turning ON S<sub>3</sub> and S<sub>4</sub>, the series inductance is reduced below  $L_m$  which makes the input matching feasible. A  $g_m$ -boosted [32] common-gate input stage [8], [9] is used in the LNA.  $R_{i,\text{LNA}}$  is designed to be lower than 50  $\Omega$  to reduce the input transistor's noise contribution. In simulation, the  $\pi$ -matching network degrades the LNA NF only by 0.8/1 dB in the 28-/37-GHz bands.

## B. Two-Way Power Combining PA

1) PA Core: RF and mm-wave PAs in the low-voltage CMOS technology achieve high output power by coherently combining the outputs of multiple PA units. In such power combining PAs, a subset of PA units can be turned OFF to improve back-off efficiency at lower input power [33], [34]. In this work, two-way power combining is implemented using a transformer-based power combining network [see Fig. 5(c)]. As explained in Section IV-A, the PA can be configured into the HP or LP modes. Fig. 2(c) and (d) shows that using the LP configuration at lower input power, PA back-off efficiency can be significantly improved, which in turn enhances the superiority of FC-HBF or DBF architectures. However, to implement dynamic load modulation and back-off efficiency improvement, dynamic switching between HP and LP modes [33], [34] is required, which was not implemented in this work.

The output stage of each PA unit is biased in deep Class-AB (around Class-B) to improve peak efficiency and back-off efficiency over Class-A [31]. Moreover, as the third-harmonic current from the output stage transistors can be substantially reduced by biasing them in Class-B [31], the output 1-dB compression point can also be pushed closer to the peak output power, thereby achieving flatter amplitude-to-amplitude (AM-AM) characteristics. In addition, the sweet-spot biasing around Class-B also reduces the amplitude-to-phase (AM-PM)

distortion [34], [35] even without varactor-based gate capacitance nonlinearity compensation [34]. However, the Class-B output stage suffers from low gain. Therefore, three driver stages with Class-AB biasing are used in each PA unit to ensure high overall PA gain. The transconductors in the output stage and driver stages #1 and #2 (see Fig. 4) use pseudodifferential NMOS pairs without cascode devices for improved linearity at a scaled power supply and with cross-coupled  $C_{\rm GD}$  neutralization [34], [35] for improved stability. Driver stage #3 (in Fig. 4) uses a pseudo-differential pair with cascode for better output to input isolation. All inter-stage matching networks use dual-band coupled resonator loads, whose design is explained in Section IV-B2. The common-mode stability of the PA is greatly improved by leaving the secondaryside center-tap of the transformers open (see Fig. 4). This restricts the common-mode feedback current to flow to the previous stage by providing a high common-mode impedance

2) Dual-Band Loads and Gain Equalization: The transimpedance  $(Z_{21})$  of a transformer-coupled resonator was used in [8] and [37]–[39] to realize wideband loads and in [9] to realize a dual-band load.  $Z_{21}$ -based dual-band loads are extensively used in this PA design and also in other parts of the front-end. In addition to  $Z_{21}$ , we show here that the driving point impedance  $(Z_{11})$  of a transformer-coupled resonator also has a dual-band characteristic; this property is used in driver stage #3 (see Fig. 4) of the PA. Equation (4) reveals that both  $Z_{11}$  and  $Z_{21}$  of a symmetrically coupled resonator  $[L_1 = L_2 = L$  and  $C_1 = C_2 = C$  in Fig. 6(a)] have identical complex pole pairs, and therefore can both be used as concurrent dual-band loads where the center frequencies of the two bands coincide with the two pole frequencies in the following equation:

$$Z_{11}(s) = \frac{\omega_0^2 L\left(s + \frac{\omega_0}{Q}\right) \left(s^2 + \frac{\omega_z}{Q_z}s + \omega_z^2\right)}{\left(s^2 + \frac{\omega_{p1}}{Q_{p1}}s + \omega_{p1}^2\right) \left(s^2 + \frac{\omega_{p2}}{Q_{p2}}s + \omega_{p2}^2\right)}$$

$$Z_{21}(s) = \frac{kL\omega_{p1}^2\omega_{p2}^2 \times s}{\left(s^2 + \frac{\omega_{p1}}{Q_{p1}}s + \omega_{p1}^2\right) \left(s^2 + \frac{\omega_{p2}}{Q_{p2}}s + \omega_{p2}^2\right)}$$
(4)

where

$$\omega_{p1,p2} = \frac{\omega_0}{\sqrt{1 \pm k}}, \quad \omega_z = \frac{\omega_0}{\sqrt{1 - k^2}}, \quad \omega_0 = \frac{1}{\sqrt{LC}}$$

$$Q_{p1,p2} = Q\sqrt{1 \pm k}, \quad Q_z = Q\frac{\sqrt{1 - k^2}}{1 + k^2}, \quad Q = \frac{\omega_0 L}{R_s}.$$

In the context of dual-band design,  $Z_{11}$ - and  $Z_{21}$ -based loads have the following advantages and disadvantages.

- 1) In the  $Z_{21}$ -based design, the drive port and the load port are isolated. Hence, the parasitic capacitance of the drive and load ports can be separately absorbed in the two sides of the coupled resonator. Therefore, the  $Z_{21}$ -based design can support higher parasitic capacitance while using an identical transformer to achieve similar peak gain.
- 2) The  $Z_{21}$ -based design with two transformer feed points at the opposite sides of the transformer coil can be adopted to realize a long and skinny layout for each

- stage [8], [9]. On the other hand, in a  $Z_{11}$ -based design, as the driver and the load are both connected to the same port of the transformer,  $Z_{11}$  loads can be adopted in a scenario where the signal path takes a 90° turn (driver stage #3 Fig. 4).
- 3) In contrast to a  $Z_{21}$ -based design where the high-frequency resonance mode (at  $\omega_H$ ) always has worse gain than the low-frequency mode (at  $\omega_L$ ), the  $Z_{11}$ -based design with asymmetric resonator can achieve higher gain either at  $\omega_H$  or at  $\omega_L$ . For an asymmetric resonator with desired dual-band operation at  $\omega_H$  and  $\omega_L$ , the resonator's design parameters  $\omega_1 = 1/\sqrt{L_1C_1}$  and  $\omega_2 = 1/\sqrt{L_2C_2}$  can be chosen according to the following equations where k should be less than or equal to  $(\omega_H^2 \omega_L^2)/(\omega_H^2 + \omega_L^2)$ :

$$\omega_{1}^{2} = \frac{1}{L_{1}C_{1}} = \frac{(1-k^{2})}{2}$$

$$\times \left[\omega_{H}^{2} + \omega_{L}^{2} \mp \sqrt{(\omega_{H}^{2} + \omega_{L}^{2})^{2} - \frac{4\omega_{H}^{2}\omega_{L}^{2}}{(1-k^{2})}}\right]$$

$$\omega_{2}^{2} = \frac{1}{L_{2}C_{2}} = \frac{(1-k^{2})}{2}$$

$$\times \left[\omega_{H}^{2} + \omega_{L}^{2} \pm \sqrt{(\omega_{H}^{2} + \omega_{L}^{2})^{2} - \frac{4\omega_{H}^{2}\omega_{L}^{2}}{(1-k^{2})}}\right]. \quad (5)$$

Please note that  $\omega_1$  and  $\omega_2$  have two solutions—one for  $\omega_1 > \omega_2$  and the other for  $\omega_1 < \omega_2$  (shown in Fig. 6(b) in the two sides of the dotted line). To find the design space for achieving higher or lower amplitudes at  $\omega_H$  or  $\omega_L$ , the  $Z_{11}$ and  $Z_{21}$  amplitude responses are simulated for an asymmetric resonator with  $L_1 = L_2 = 200$  pH and  $Q_1 = Q_2 = 20$ . The ratio of two peak amplitudes at  $\omega_L$  and  $\omega_H$  is plotted versus k in Fig. 6(b) in dB scale for  $f_L = 28$  GHz and  $f_H = 38$  GHz. It can be seen that the amplitude ratio in case of  $Z_{21}$  is always greater than 0 dB, where in case of  $Z_{11}$  it can be either greater or less than 0 dB. Two exemplary amplitude responses for two operating regions of  $Z_{11}$  are shown in Fig. 6(c). Therefore, it can be concluded that the  $Z_{11}$ -based design can help equalizing the gain at high- and low-frequency bands in a dual-band design. The aforementioned property is used in the PA design to reduce the gain difference in the two operating bands using  $Z_{11}$  in one driver stage and  $Z_{21}$  in other driver stages.

3) Dual-Band Second-Harmonic Short: A PA output stage biased in deep Class-AB or in Class-B generates significant second-harmonic currents under large-signal condition [31]. The second-harmonic current, when flows through the load impedance, creates a significant second-harmonic voltage at the output node. This can degrade  $P_{\rm sat}$ , PAE, and AM-PM distortion of the PA [35], [40], [41]. Spirito *et al.* [40] and Ye *et al.* [41] show that the performance degradation can be overcome by placing harmonic traps (load network that provides the harmonic current a low impedance path to ground) at the PA output node. However, previous techniques used a single-frequency second-harmonic trap; as pointed out in [35], these techniques are difficult to incorporate in

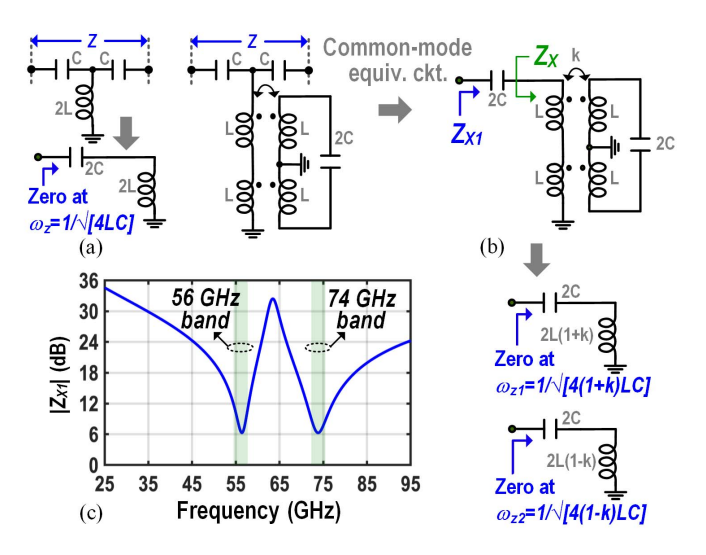


Fig. 7. (a) Single-band second-harmonic trap. (b) Dual-band second-harmonic trap network used in this prototype design in Fig. 4. (c) Simulated dual-band second-harmonic short response.

wideband or multi-band designs. A conventional harmonic trap design is shown in Fig. 7(a). To support a 28- and 37-GHz operation, a significant amount of frequency tuning is required, thereby degrading the quality factor of the trap across frequency. Moreover, conventional harmonic-trap networks cannot support concurrent dual-band second-harmonic trapping.

A novel second-harmonic trap network is introduced next. It uses a transformer-coupled resonator to realize a dual-band short, as shown in Fig. 7(b). In a differential PA design, the second-harmonic current appears as common-mode signal. The common-mode equivalent network of the proposed design is shown in Fig. 7(b), where the common-mode input impedance ( $Z_{X1}$ ) of the network can be calculated as follows:

$$Z_{X1}(s) = 2L(1 - k^2) \times \frac{\left(s^2 + \frac{\omega_{z1}}{Q_{z1}}s + \omega_{z1}^2\right) \left(s^2 + \frac{\omega_{z2}}{Q_{z2}}s + \omega_{z2}^2\right)}{s\left(s^2 + \frac{\omega_0}{Q_0}s + \omega_0^2\right)}$$
(6)

where

$$\omega_{z1} = \frac{1}{\sqrt{4(1+k)LC}}, \quad \omega_{z2} = \frac{1}{\sqrt{4(1-k)LC}}$$

$$Q_{z1,z2} = Q_0\sqrt{(1\pm k)}, \quad Q_0 = \omega_0 L/R, \quad \omega_0 = 1/\sqrt{4LC}.$$

Equation (6) reveals that  $Z_{X1}$  has two zeroes that concurrently provide low-impedance paths at two frequencies. The proposed network is equivalent to a series LC network where the inductance  $[Z_X$  in Fig. 7(b)] concurrently takes two different values at two resonant modes of the transformer (even and odd modes). A simulated dual-band second-harmonic trap response is shown in Fig. 7(c) for a dual-band 56-/74-GHz short. The second-harmonic short reduces the second-harmonic current in the PA's output stage by  $\sim 3\times$ .

#### C. Bidirectional Self-Neutralized Phase-Invariant PGA

Unlike conventional phased-array transceivers [1]–[3] where separate PGAs have been used in the TX and RX paths, all PGAs in this prototype are designed to share passives in TX and RX configuration for compactness. Compact designs not only reduce the area and cost but also eliminate losses due to long interconnects. A straightforward way to realize a bidirectional PGA is by using a single programmable transconductor in conjunction with signal-path switches to reverse the direction of signal flow. However, in such a design, the signal-path switches can cause significant loss at mm-wave frequency while also degrading PGA linearity.

- 1) Bidirectional PGA Design: To overcome the aforementioned problem, a bidirectional PGA design is introduced that avoids signal-path switches, as shown in Fig. 8. Here, two back-to-back programmable transconductors are used, one for each signal path direction. To configure for forward (reverse) signal flow, the forward (reverse) programmable transconductor is turned ON, while the reverse (forward) transconductor is turned OFF. The programmable transconductors use techniques proposed in [8] to achieve phase-invariant gain control. In addition to turning ON/OFF the transconductor cells by controlling the tail-bias of the differential pair, separate biasing network for the transconductors' gate-bias is also used to enable either the forward or the backward path. Although the proposed technique uses twice the number of active devices and increases the capacitance at each node by the OFF-state capacitance of each path, it eliminates signal-path switch loss.
- 2) Neutralization Technique: A differential amplifier without cascode devices experiences output-to-input feedback through the gate-to-drain capacitance  $(C_{\rm GD})$  of the input pair. An explicit cross-coupled capacitance pair can be used to neutralize this feedback, thereby improving differential-mode stability. Neutralization based on this principle is implicitly available in the proposed bidirectional PGA topology, because  $C_{\rm GD}$  of the OFF-state transconductor in the reverse/forward path cancels the feedback through the ON-state transconductor in the forward/reverse path (see Fig. 8). Transconductors in the forward and reverse paths should be oppositely connected, as shown in Fig. 8 (the feedback path from one output to both the input nodes is highlighted in green). It is important to note that feedback capacitances from the ON and OFF paths in the self-neutralized bidirectional architecture matches well over PVT, thereby providing PVT-invariant differential-mode stability.

The common-mode stability of the proposed bidirectional PGA topology is improved by using switches  $S_{C1}$ – $S_{C4}$  at the center taps of the coupled resonators that selectively connect to the power supply or leave it open to reduce the common-mode feedthrough [36]. As shown in Fig. 8, switches  $S_{C1}$  and  $S_{C3}$  ( $S_{C2}$  and  $S_{C4}$ ) are turned ON for the forward (reverse) configuration.

## D. Bidirectional Per-Stream Complex-Weighting

The design of the per-stream, bidirectional complex weights is described with reference to Fig. 4. A pair of bidirectional 5-bit (including sign bit) PGAs is used in each

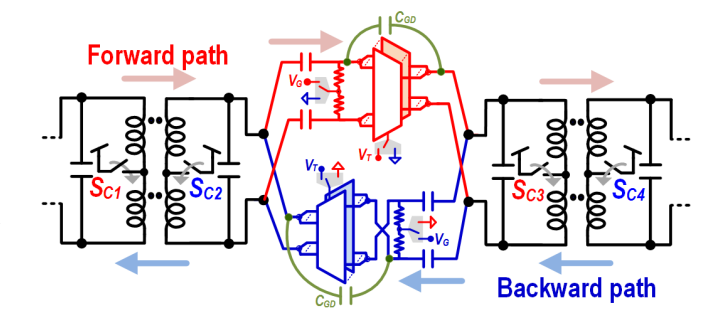


Fig. 8. Bidirectional programmable gain stage. Forward path is shown in red and backward path is shown in blue. Feedback path from both the output ports to one of the input port is highlighted in green.

stream to realize the Cartesian complex weights. In the TX path, the inputs to the PGA pair can be generated locally using quadrature hybrids (one per stream), or can be generated globally before splitting to other elements by extending the Cartesian combining [10] technique. The outputs of the PGAs in the complex weight are combined in the TX path using a bidirectional current-mode combiner. Similarly, in the RX path, the inputs of the PGAs in the complex weight are generated using a voltage-mode splitter, and the outputs from the PGA pair can be combined either locally [30] or globally [9]. In addition, fine gain control ( $\sim$ 0.3 dB LSB) in each stream is achieved using an additional 5-bit (without sign) bidirectional PGA, and fine phase control ( $\sim 0.5^{\circ}$ ) is achieved using a 5-bit digitally switchable capacitor in the coupled resonator load of the PGA, as shown in Fig. 4. Fine gain and phase control enables accurate complex-weighting and accurate SIC in the STAR mode. Finally, to improve the common-mode stability, switches S<sub>5</sub>-S<sub>8</sub> in Fig. 4 are incorporated in two streams.

### E. Splitter/Combiner and Dual-Band SIC

The two bidirectional streams are interfaced with the PA and the LNA using a coupled resonator. One side (say the primary side) of the coupled resonator is connected to two PA slices and the LNA, and the secondary side is connected to both streams (see Fig. 4). Fig. 9(a)–(c) shows how the interface can be configured in the TX, RX, and STAR modes. No signal-path switches are used in this design. In the TX mode, the LNA is turned OFF and both streams are configured to transmit [see Fig. 9(a)]. The signal currents from the two PGAs from the two streams are combined in the secondary side of the coupled resonator. The voltage developed in the primary side splits into two PA slices through the voltage-mode splitter. In the RX mode, both PA slices are turned OFF and both streams are configured to receive [see Fig. 9(b)]. The signal current from the LNA stage #2 transconductor is fed into the primary side of the coupled resonator. The voltage developed on the secondary side is split into two streams by the voltage-mode splitter by reusing the same passive structure that is used for current combining in the TX mode.

In the STAR mode of operation, the per-element SIC is required in the RX beamformer. In this mode, both PA slices

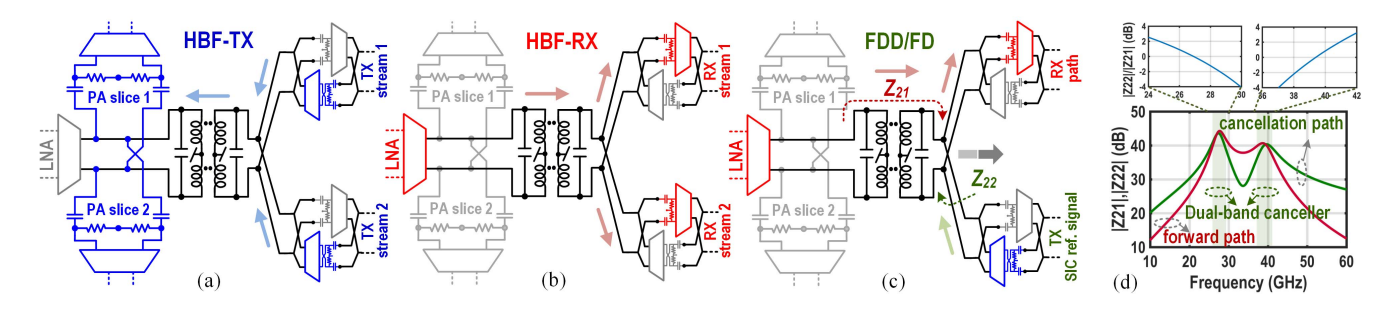


Fig. 9. LNA/PA and stream #1/#2 interface splitter combiner network in (a) two-stream FC-HBF TX mode, (b) two-stream FC-HBF RX mode, and (c) FDD or FD beamforming mode with SIC. (d) Magnitude response of the coupled resonator load in the forward signal path  $(Z_{21})$  and in the cancellation path  $(Z_{22})$  showing the capability of dual-band SIC.

are turned OFF. One stream is configured as receive for the desired input, and the other stream is configured as transmit to perform SIC [see Fig. 9(c)]. The signal current from the LNA's stage #2 transconductor is inserted into the primary side of the coupled resonator, and the signal current from the SIC path stream is fed into the secondary side. After SIC is performed inside the coupled resonator, the voltage developed in the secondary side drives the receive stream. Therefore, in the STAR mode, the forward path sees the trans-impedance  $Z_{21}$  of the resonator as the load, while the SIC path sees the drivingport impedance  $(Z_{22})$  as the load [see Fig. 9(c)]. As described in Section IV-B, both the driving-port impedance and the transimpedance of a coupled resonator have dual-band behavior. Equation (7) shows how the gain through both the paths can be equalized in both bands by selecting moderate coupling and high kQ product. This is supported by the simulation shown in Fig. 9(d)

$$\left| \frac{Z_{11}(j\omega)}{Z_{21}(j\omega)} \right|_{\omega_{p1,p2}} \approx \left| \frac{\omega_z^2 - \omega^2 + j\frac{\omega_z}{Q_z}\omega}{k\omega_{p1}^2\omega_{p2}^2/\omega_0^2} \right|_{\omega_{p1,p2}} = \sqrt{1 + \left(\frac{1}{kQ} \times \frac{1 + k^2}{\sqrt{1 \pm k}}\right)^2} \approx 1.$$
(7)

Thus, both the receive path and the SIC path can achieve reasonable gain concurrently in both bands, thereby enabling cancellation in either of the two bands. The forward and the cancellation paths can be at two different frequencies (in the FDD mode) or can be in the same frequency band (in the FD mode). It should be noted that the noise from the SIC path can degrade the RX NF in FDD/FD configuration. However, because the SIC is performed after two LNA stages in the RX chain, NF degradation is minimal (0.4/0.5 dB in the 28-/37-GHz band in simulation) in this design.

# V. MEASUREMENT RESULTS

The multi-band transceiver front-end prototype is designed and fabricated in a 65-nm CMOS process (see Fig. 10) and occupies 0.4 mm × 1.2 mm (i.e., 0.48-mm<sup>2</sup> core area) including AIN, LNA, PA, and two-stream complex-weighting for a single-antenna element. Maximal compactness is achieved by sharing passive structures in all modes. Custom passives are designed in such a way that they minimize the slice height to facilitate compact multi-element integration [8], [9].

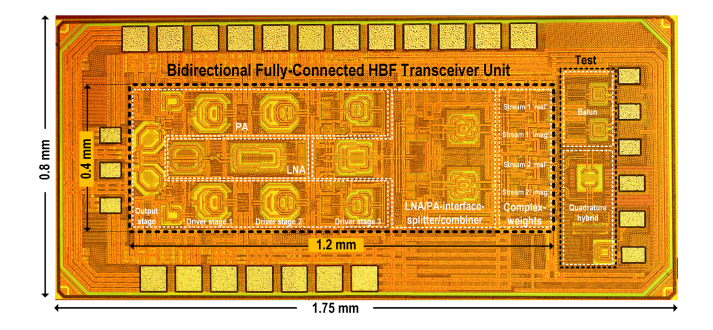


Fig. 10. Die micrograph of 28-/37-/39-GHz multi-mode bidirectional hybrid/digital beamforming front-end prototype.

The single-element transceiver consumes 37.6 and 116.2 mA in the RX and TX modes, respectively, from a 1-V  $V_{DD}$  (17.6 mA in LNA, 96.2 mA in PA, and 20 mA in complex weights). All measurements below were performed by on-wafer probing.

# A. Single-Element Transmitter and Receiver Characterization

The TX and RX modes of a single element are characterized by turning on only the I (or Q) path PGA of stream #1 (see Fig. 4) in full gain settings. As shown in Fig. 11(a), the receiver achieves 16.1/10.9/8.3 dB conversion gain, 6.2/7.0/7.9 dB NF, -13.2/-15.1/-12.8 dB  $S_{11}$ , and -15.7/-14.5/-12.8 dBm input-referred 1 dB compression point at 28/37/39 GHz. Fig. 11(b) shows that the transmitter gain is 28.5/26.2/20.3 dB at 28/37/39 GHz. The input-referred IP3 is -6.8/-5.8/-3.4 dBm (-2.7/-2.4/-0.8 dBm) in the RX mode for full PGA gain (PGA gain 6 dB lower than the maximum), and the output-referred IP3 is 23/24.5/22.5 dBm in the TX mode at the 28/37/39 GHz band. The dual-band gain peaking is more prominent in the TX due to the use of  $Z_{11}$  of coupled resonator (that has a complex zero between the two complex poles) as load in a PA driver stage. Note that the TX gain is higher than the RX gain in this design. The front-end slice in this work is designed to be inserted as is into a complete HBF. The PA gain is designed to be high to overcome the expected losses in the TX splitting network in an HBF. In contrast, in the RX path of an HBF, the signals from multiple elements are combined, and hence, the signal strength

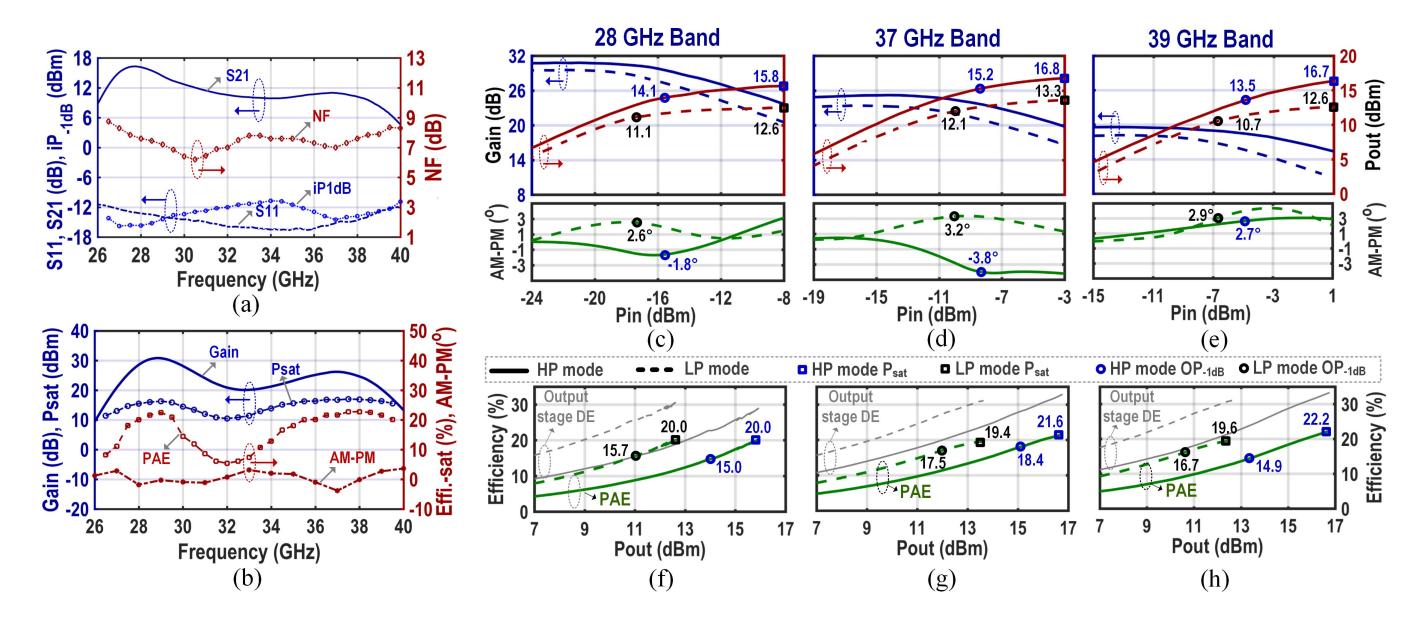


Fig. 11. (a) RX path  $S_{21}$ ,  $S_{11}$ , NF, and  $iP_{1dB}$  versus frequency. (b) TX path gain, saturation power, PAE, and AM-PM distortion versus frequency. Large-signal PA gain, output power, and AM-PM distortion over input power in (c) 28 GHz, (d) 37 GHz, and (e) 39 GHz bands. PA efficiency versus output power in (f) 28 GHz, (g) 37 GHz, and (h) 39 GHz bands.

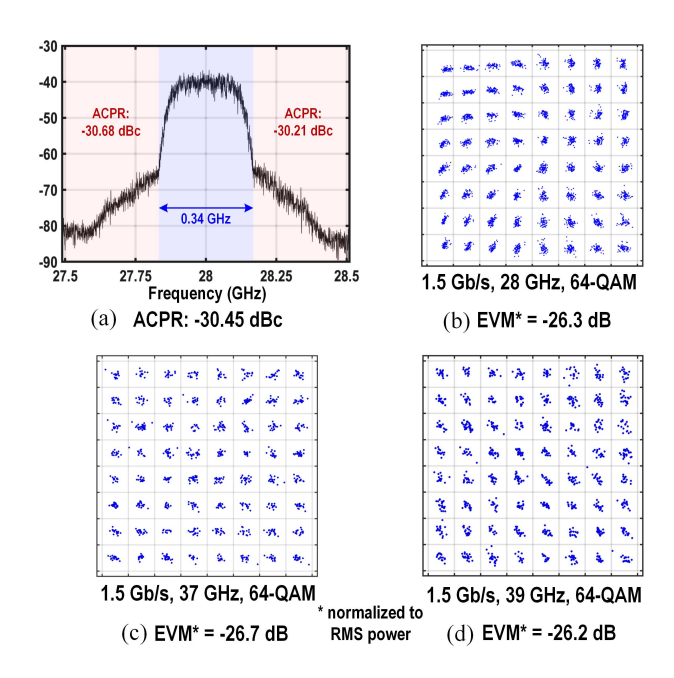


Fig. 12. (a) Measured TX ACPR. TX constellation error-vector magnitude (EVM) at (b) 28-, (c) 37-, and (d) 39-GHz bands.

increases down the chain. Therefore, the LNA is designed with relatively low gain.

Next, in the TX mode, the PA is characterized for large-signal continuous-wave (CW) performance.  $P_{\rm sat}$ , PAE, and AM-PM over the 26–40-GHz frequency range are shown in Fig. 11(b). Detailed large-signal performance with 28, 37, and 39 GHz CW inputs is shown in Fig. 11(c)–(h). In the HP TX mode [solid line in Fig. 11(c)–(h)], 15.8/16.8/16.7 dBm  $P_{\rm sat}$ , 20.0%/21.6%/22.2% peak PAE, 28.9%/32.9%/33.3% output stage drain efficiency, 14.1/15.2/13.5 dBm  $P_{\rm 1dB}$ ,

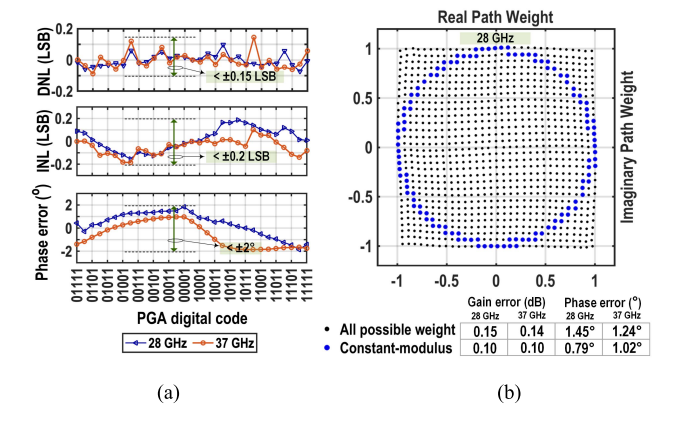


Fig. 13. (a) PGA DNL, INL, and phase error versus digital control code for the 28- and 37-GHz bands. (b) Complex-weight constellation measurement in the 28-GHz band and measured gain and phase error for both the 28- and 37-GHz bands.

15.0%/18.8%/14.9% PAE at  $P_{\rm 1dB}$ , and  $-1.8^{\circ}/-3.8^{\circ}/2.7^{\circ}$  AM-PM distortion at  $P_{\rm 1dB}$  are achieved at 28/37/39 GHz. As shown in Table II, compared with the recent multi-band standalone PAs, this work achieves better PAE at  $P_{\rm 1dB}$  than [35] while also achieving better AM-PM across all bands than [42]. At 6-dB power back-off, the measured PA power consumption ( $P_{\rm dc}$ ) decreases by ~40% (~50% for the output stage only, which matches ideal Class-B behavior) compared with  $P_{\rm dc}$  at  $P_{\rm sat}$ , thereby achieving lower back-off  $P_{\rm dc}$  than Class-A PA. This paves the way for system efficiency improvement with the FC-HBF design.

The PA is measured next in the LP mode by turning OFF one PA unit with primary side  $S_3$  ON [see Fig. 5(d)]. The CW performance is shown in Fig. 11(c)–(h), dashed line. The LP mode achieves  $\sim$ 4 dB lower gain and output power than the HP mode with similar PAE. This points to the

TABLE II
COMPARISON AGAINST STATE-OF-THE-ART BEAMFORMERS, PAS, AND SINGLE-ANTENNA SIC

			This Work		Dunworth [4] ISSCC'18	nt 4-element multi-band		Sadhu [1] JSSC'17	Kim [3] JSSC'18	Kibaroglu [2] JSSC'18	Mondal [8] JSSC'18	Vigilante [35] JSSC'18		Hu [42] ISSCC'17		Dinc [44] JSSC'16		
	Functionalities	FC-HB + FD/FI	and bi-dire F T/R fro DD mode Intenna sy	nt-end SIC for	12-element dual-pol T/R with packaging			16-element dual-pol T/R with packaging	4-element dual-pol T/R with packaging	4-element T/R phased array	8-element FC-HBF RX	Multi-band Class-AB PA			Multi-band Doherty PA			SIC in single- antenna system
. [	Technology	65	nm CMO	S	28nm CMOS 65nm CMOS		130nm SiGe	28nm CMOS	180nm SiGe	65nm CMOS	28nm CMOS			130nm SiGe			45nm SOI	
<b>1</b>	Freq. (GHz)	28	37	39	25-30.5	28	37	28	28	28-32	25-30	30	40	50	28	37	39	57-66
	RX Gain (dB)	16.1	10.9	8.3	24ª	33a	26.5ª	34ª	39ª	20	34ª	-	-	-	-	-	-	40
×	NF <sub>min</sub> (dB)	6.2	7.0	7.9	4.4ª	5.7a	8.5ª	6	6.7ª	4.6	7.3ª	-	-	-	-	-	-	4
¥	S11 (dB)	-13.2	-15.1	-12.8	<-10	<-10	<-15	-	-	<-10	<-8	-	-	-	-	-	-	<-7
	iP <sub>1dB</sub> (dBm)	-15.7	-14.5	-12.8	-	-30ª	-23ª	-22.5	-	-22	-29ª	-	-	-	-	-	-	-32
$\downarrow$	oP <sub>1dB</sub> (dBm)	0.4	-3.6	-4.5	-	3a	3.5a	9.7a	-	-2	5ª							8
1	TX Gain (dB)	28.5	26.2	20.3	44a	-	-	32ª	-	14	-	19*	20.8	19*	18.2	17.1	16.6	-
	P <sub>SAT</sub> (dBm)	15.8	16.8	16.7	14	-	-	16	10.5	<13	-	16.6	15.9	15.1	16.8	17.1	17	11-15
$\succeq$	PAE@ Psat (%)	20.0%	21.6%	22.2%	-	-	-	-	-	-	-	24.2	18.4	14.9	20.3	22.6	21.4	15.3
TI	P <sub>1dB</sub> (dBm)	14.1	15.2	13.5	12	-	-	13.5	9.5	<11.7	-	13.4	11.1	10.9	15.2	15.5	15.4	-
	PAE@ P <sub>1dB</sub> (%)	15.0%	18.8%	14.9%	-	-	-	-	-	-	-	12.6	7.5	7.0	19.5	21.6	20.7	-
1	AM-PM@ P <sub>1dB</sub> (°)	-1.8°	-3.8°	2.7°	-	-	-	-	-	-	-	-0.7	-0.26	0.45	10	1.3	3.9	-
â	SICPEAK (dB)	36			-	-		-	-	-	-	-		-		21-		
힣	SIC BW (GHz)	0.5 (26 dB SIC)		-	-		-	-	-	-	-			-			1	
Ť	Power (mW)#	37.6 (R	X), 116.2	(TX-DC)	42°(R),90°(T)	52.5t	(RX)	206b(R),287b(T)	50°(R),85°(T)	130(R),200(T)	27.5b (RX)	170 (PA-DC)		C)	65 (PA-DC)		111(R),206(T)	
	Area (mm²)#	0.48		1.16∘	0.46b		2.59₺	0.910	2.9	0.32b	0.16		1.735			4.42		

<sup>\*</sup>Single channel \*Estimated -RF SIC Including \*down-conversion bdown-conversion and partial LO generation cdown-convertion and full LO generation

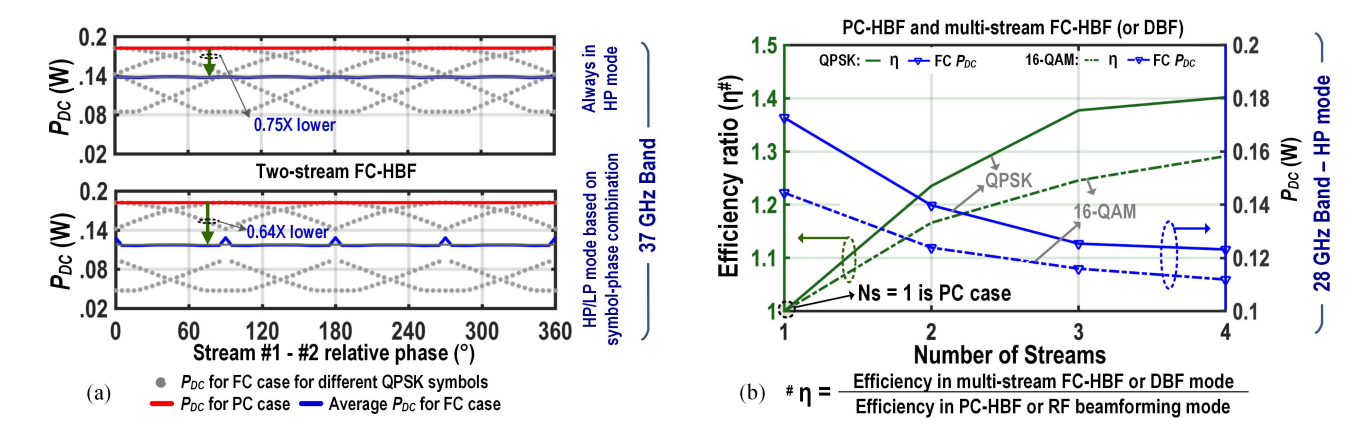


Fig. 14. (a) PA power consumption in the PC-HBF and two-stream FC-HBF modes for all possible QPSK symbols across all possible relative phases between two streams in the FC case. (b) PA power consumption in the FC-HBF mode and efficiency ratio of the FC-HBF over PC-HBF multi-stream TX for QPSK and QAM modulation schemes.

feasibility of obtaining substantial back-off efficiency improvement by implementing dynamic mode switching.

Finally, Fig. 12(a) and (b) shows a measured TX EVM of -26.3 dB (normalized to rms power) and ACPR of -30.45 dBc (0.34 GHz RF-BW) at 7.1 dBm average output power for 1.5-Gb/s 64-QAM modulation with root-raised-cosine filtering (roll-OFF factor 0.35) in the 28-GHz band HP mode. In the LP mode at 4 dBm of average output power, -26.5 dB EVM and -31.1 dBc ACPR are achieved for the same modulation. As shown in Fig. 12(c) and (d), the measured EVM in the HP mode at 37 and 39 GHz is -26.7 dB and -26.2 dB at 8 dBm and 6.5 dBm average output power, respectively.

# B. Complex-Weight Characterization

The linear phase-invariant PGA design, originally proposed in [43] and extended in this work for bidirectional complex-weighting, is characterized next for all possible 5-bit (includ-

ing sign bit) programmable settings. As shown in Fig. 13(a), the 5-bit PGA achieves differential and integral non-linearity less than  $\pm 0.15$  LSB and  $\pm 0.2$  LSB, respectively, and phase variation of  $\pm 2^{\circ}$  over all gain settings in the 28- and 37-GHz bands, respectively. Fine-grained RF-PGA design with minimal non-ideality ensures high-resolution complex-weighting [961 distinct possible settings in Fig. 13(b)] with excellent rms gain and phase error performance of 0.15 dB (0.10 dB) and 1.45° (0.79°), respectively, for all possible complex-weight settings (constant-modulus weight settings) in the 28-GHz band. Gain and phase error performance in the 37-GHz band are also tabulated in Fig. 13(b).

# C. PC-HBF Versus FC-HBF/DBF Mode Energy Efficiency

The single-element two-stream front-end is characterized in one-stream PC-HBF and two-stream FC-HBF modes for identical peak output transmit power (this implies identical spectral efficiency, consistent with the conclusions

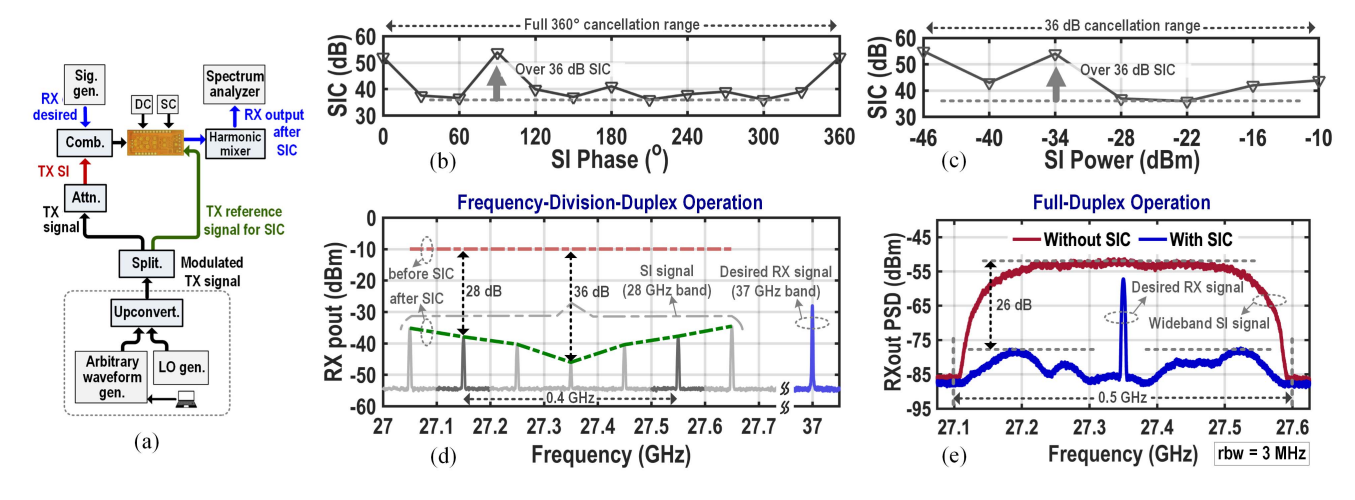


Fig. 15. (a) FDD/FD mode measurement setup. (b) SIC versus SI signal phase. (c) SIC versus SI signal power. (d) FDD mode SIC with the two-tone interferer in the 28 GHz band and the desired RX tone in the 37 GHz band. (e) FD mode SIC with wideband modulated SI and desired tone both in the 28 GHz band.

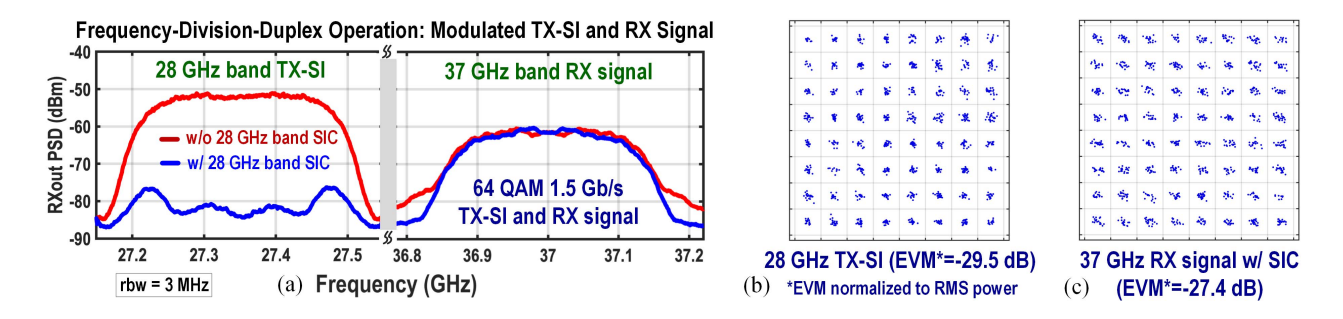


Fig. 16. FDD mode operation with 28 GHz band modulated TX-SI and 37 GHz band modulated desired RX signal. (a) Signal spectrum at both bands w/ SIC ON and OFF. (b) Constellation of the TX-SI received in the RX path w/ the SIC OFF. (c) Constellation of the desired RX signal w/ the SIC ON.

in Section II). In the FC-HBF mode, the DC power consumption of PA ( $P_{\rm dc}$ ) is measured for all possible combinations of QPSK symbols in both streams for two configurations of the PA: 1) always in the HP mode and 2) switched between the HP and LP modes depending on the output power requirement for current set of symbols. The above measurement is then repeated for all possible relative phases between two streams because the relative phase can vary from element to element in a full FC-HBF array. As shown in Fig. 14(a), for all relative phase settings in the two-stream FC-HBF mode,  $P_{\rm dc}$  reduces to  $\sim 0.75 \times$  and  $\sim 0.64 \times$  of the PC-HBF mode, respectively, for configurations 1) and 2).

Next, the PA performance in the multi-stream FC-HBF (or DBF) mode is characterized using an appropriate baseband equivalent signal (after complex-weighting and combining from each stream for a single element) generated using arbitrary waveform generator (AWG), upconverted, and applied to the chip. In this experiment, the peak transmitted output power is assumed to be constant in PC and FC cases across different number of streams. As predicted in Section II, under this constraint the PA power consumption in the FC-HBF case reduces with the number of streams [see in Fig. 14(b)] due to the requirement of the lower average output power in the FC case than in the PC case. Moreover, the efficiency ratio of the FC over the PC case improves with the number of streams for different modulation schemes [QPSK and

16-QAM in Fig. 14(b)]. The above set of measurement showcases the superior energy efficiency of the FC-HBF TX compared with the PC-HBF TX.

#### D. FDD/FD Mode Characterizations

The SIC in the FDD/FD mode is characterized using the setup shown in Fig. 15(a) where the concept of Fig. 1(e) is emulated for a single element using external components. First, the SIC performance is verified for a single-tone TX SI without RX input. The signal phase and the power of the TX SI at the RX input are swept using external variable attenuators and phase shifters, respectively, with the TX reference signal for the SIC kept unchanged. The RF canceller settings (both coarse and fine) for the best possible SIC are set automatically for each case of the TX SI. An automated benchtop grid search algorithm is used that searches for the gain and phase settings of the canceller path with a coarse step in the first iteration, and with a finer step around the first step settings in the second iteration. It can be seen from Fig. 15(b) and (c) that over 36 dB SIC can be achieved for a narrowband TX SI for full 360° range of SI phase and 36 dB range of SI power. With the LNA  $iP_{1\,dB}$  of -10 dBm in this design, upto 20 dBm of TX power can be supported for 30 dB antenna isolation.

Next, the FDD mode operation is characterized using a desired RX tone at 37 GHz and a two-tone TX SI placed

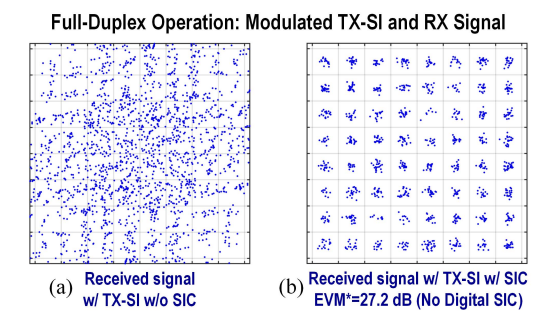


Fig. 17. FD mode received constellation with the RF domain: (a) SIC OFF and (b) SIC ON.

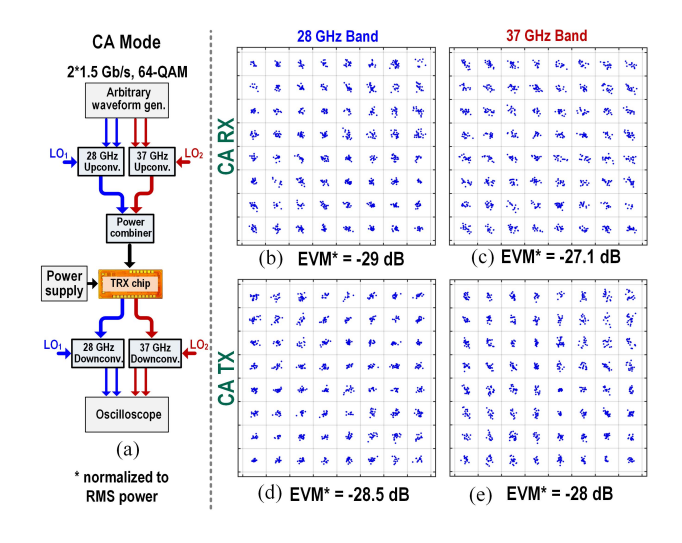


Fig. 18. (a) CA mode measurement setup. Constellation measurement for the CA-RX mode in (b) 28- and (c) 37-GHz bands. Constellation measurement for the CA-TX mode in (b) 28- and (c) 37-GHz bands.

near 28 GHz. The SIC setting is first set once for maximum cancellation at the band center (at 27.35 GHz for this experiment) using the automated grid search algorithm, and the spacing between two SI tones is then swept to measure SIC performance over the interferer BW. As shown in Fig. 15(d), the 36 dB SIC is achieved at the band center and the 28 dB SIC is achieved for a two-tone interferer (simultaneously for both tones) with 400 MHz spacing. Finally, FD operation is demonstrated using a wideband modulated TX SI in the 28 GHz band and a desired RX tone in the same band (placed at the center of the TX SI) using the setup shown in Fig. 15(a). Fig. 15(e) indicates that the RX output is dominated by the TX interferer and the desired tone is indistinguishable when the RF canceller is OFF. However, it can be seen that by turning ON the RF canceller, over 26 dB SIC is achieved for the full 500 MHz of interferer BW and the desired RX tone becomes clearly distinguishable. Similar to the cancellation performance at the 28 GHz band, the dual-band SIC technique also achieves 26 dB SIC for a two-tone test with 400 MHz spacing and over 25 dB SIC for a 500 MHz BW TX SI at the 37 GHz band. As shown in Table II, compared with the mm-wave FD work for the

single-antenna system in [44], this work achieves superior RF-domain SIC for identical fractional BW of TX self-interferer.

Finally, the operation in the FDD and FD modes is demonstrated with modulated TX-SI signal and desired RX signal, both using a 64-QAM 1.5 Gb/s modulation scheme. In both modes, the peak power of TX-SI is  $-16 \, dBm$ , assuming a peak TX output power of 14 dBm and antenna isolation of 30 dB. The designed RX can support the peak desired signal power of up to -16 dBm ( $iP_{1\text{dB}}$  of the RX), where the peak power of the composite signal still stays below  $iP_{1dB}$  of the LNA (i.e., -10 dBm). In the FDD mode, the 28 GHz band TX-SI and the 37 GHz band desired signal with identical average input power level (peak power is set as  $iP_{1 dB}$  of the LNA) are applied to the receiver input. The RX output spectrum is shown in Fig. 16(a) with the SIC ON and OFF. As shown in Fig. 16(b) and (c), TX-SI is demodulated with -29.5 dB EVM when the SIC is OFF, and the RX desired signal is demodulated with -27.4 dB EVM when the SIC is ON.

In the FD mode, both modulated TX-SI and desired RX signals in the 28-GHz band are applied to the receiver input. As shown in Fig. 17(a) and (b), the received input is corrupted with the TX-SI when the SIC is OFF, and demodulated with -27.2 dB EVM when the SIC is ON, thereby demonstrating successful FD operation.

Please note that the above measurements are performed for a single element. They demonstrate dual-band cancellation capability at RF that suppresses the dominant TX-SI component. Digital SIC is not included in these measurements. In a multi-antenna system, other sources of TX leakage may be present due to adjacent element crosstalk or coupling in the frequency translation stages, which would need further cancellation at analog or digital baseband.

#### E. CA Mode Characterizations

Inter-band CA mode performance at 28/37 GHz is characterized next in TX and RX configurations by applying two independently modulated data streams (peak power is set as  $iP_{1dB}$ ), as shown in Fig. 18(a). For 1.5 Gb/s (64-QAM) data rate in each carrier independently, the RX EVM is -29 dB and -27.1 dB, respectively [see Fig. 18(b) and (c)], and the TX EVM is -28.5 dB and -28 dB [see Fig. 18(d) and (e)] in the 28 and 37 GHz band, respectively.

#### VI. CONCLUSION

This article makes three major contributions. First, it is shown that the FC-HBF and DBF MIMO transmitters can have greater power efficiency than the conventional sub-array (PC-HBF) transmitter, despite the fact that the PAs have to handle signals with higher PAPR. It is theoretically and experimentally demonstrated that PA designs with better-than-Class-A back-off efficiency are necessary to achieve this goal. Second, a new multi-antenna simultaneous transmit—receive system architecture is introduced that provides a way to cancel SI in the RF domain on a per-element basis in an FC-HBF or DBF transceiver. With the single-element frontend prototype, the cancellation performance is characterized for one element in this work. Demonstration of SIC in a

complete multi-antenna system remains a part of future work. Third, a compact circuit topology is introduced that realizes dual-band bidirectional operation introducing minimal loss from the TX-RX switching networks. A 28-/37-/39-GHz single-element front-end prototype has been designed to showcase the system concepts introduced in this article. To this end, numerous innovative circuit techniques are introduced in this article that includes dual-band antenna interface, dual-band second-harmonic shorting network, dual-band gain equalization, bidirectional self-neutralized PGA, and so on. The front-end design can be incorporated directly in a digital or HBF transceiver system. As shown in Table II, the front-end achieves state-of-the-art performance when benchmarked against recent 28 GHz beamformers, multi-band mm-wave PAs, and single-antenna STAR system with RF-domain SIC.

#### REFERENCES

- [1] B. Sadhu *et al.*, "A 28-GHz 32-element TRX phased-array IC with concurrent dual-polarized operation and orthogonal phase and gain control for 5G communications," *IEEE J. Solid-State Circuits*, vol. 52, no. 12, pp. 3373–3391, Dec. 2017.
- [2] K. Kibaroglu, M. Sayginer, and G. M. Rebeiz, "A low-cost scalable 32-element 28-GHz phased array transceiver for 5G communication links based on a 2 × 2 beamformer flip-chip unit cell," *IEEE J. Solid-State Circuits*, vol. 53, no. 5, pp. 1260–1274, May 2018.
- [3] H.-T. Kim et al., "A 28-GHz CMOS direct conversion transceiver with packaged 2×4 antenna array for 5G cellular system," *IEEE J. Solid-State Circuits*, vol. 53, no. 5, pp. 1245–1259, May 2018.
- [4] J. D. Dunworth et al., "A 28 GHz bulk-CMOS dual-polarization phasedarray transceiver with 24 channels for 5G user and basestation equipment," in *IEEE Int. Solid-State Circuits Conf. (ISSCC) Dig. Tech. Papers*, vol. 61, Feb. 2018, pp. 70–72.
- [5] S. Kundu and J. Paramesh, "A compact, supply-voltage scalable 45–66 GHz baseband-combining CMOS phased-array receiver," *IEEE J. Solid-State Circuits*, vol. 50, no. 2, pp. 527–542, Feb. 2015.
- [6] S. Shahramian, M. J. Holyoak, A. Singh, and Y. Baeyens, "A fully integrated 384-element, 16-tile, W-band phased array with selfalignment and self-test," *IEEE J. Solid-State Circuits*, vol. 54, no. 9, pp. 2419–2434, Sep. 2019.
- [7] T. Sowlati et al., "A 60-GHz 144-element phased-array transceiver for backhaul application," *IEEE J. Solid-State Circuits*, vol. 53, no. 12, pp. 3640–3659, Dec. 2018.
- [8] S. Mondal, R. Singh, A. I. Hussein, and J. Paramesh, "A 25–30 GHz fully-connected hybrid beamforming receiver for MIMO communication," *IEEE J. Solid-State Circuits*, vol. 53, no. 5, pp. 1275–1287, May 2018.
- [9] S. Mondal and J. Paramesh, "A reconfigurable 28-/37-GHz MMSE-adaptive hybrid-beamforming receiver for carrier aggregation and multi-standard MIMO communication," *IEEE J. Solid-State Circuits*, vol. 54, no. 5, pp. 1391–1406, May 2019.
- [10] J. Paramesh, R. Bishop, K. Soumyanath, and D. J. Allstot, "A four-antenna receiver in 90-nm CMOS for beamforming and spatial diversity," *IEEE J. Solid-State Circuits*, vol. 40, no. 12, pp. 2515–2524, Dec. 2005.
- [11] H. Mohammadnezhad, R. Abedi, and P. Heydari, "A millimeter-wave partially overlapped beamforming-MIMO receiver: Theory, design, and implementation," *IEEE Trans. Microw. Theory Techn.*, vol. 67, no. 5, pp. 1924–1936, May 2019.
- [12] S. Jeon et al., "A scalable 6-to-18 GHz concurrent dual-band quad-beam phased-array receiver in CMOS," IEEE J. Solid-State Circuits, vol. 43, no. 12, pp. 2660–2673, Dec. 2008.
- [13] J. Jeong, N. Collins, and M. P. Flynn, "A 260 MHz IF sampling bit-stream processing digital beamformer with an integrated array of continuous-time band-pass modulators," *IEEE J. Solid-State Circuits*, vol. 51, no. 5, pp. 1168–1176, May 2016.
- [14] S. Jang, J. Jeong, R. Lu, and M. P. Flynn, "A 16-element 4-beam 1 GHz IF 100 MHz bandwidth interleaved bit stream digital beamformer in 40 nm CMOS," *IEEE J. Solid-State Circuits*, vol. 53, no. 5, pp. 1302–1312, May 2018.

- [15] S. Kalia, S. A. Patnaik, B. Sadhu, M. Sturm, M. Elbadry, and R. Harjani, "Multi-beam spatio-spectral beamforming receiver for wideband phased arrays," *IEEE Trans. Circuits Syst. I, Reg. Papers*, vol. 60, no. 8, pp. 2018–2029, Aug. 2013.
- [16] S. Mondal, R. Singh, and J. Paramesh, "A reconfigurable bidirectional 28/37/39 GHz front-end supporting MIMO-TDD, carrier aggregation TDD and FDD/Full-duplex with self-interference cancellation in digital and fully connected hybrid beamformers," in *IEEE Int. Solid-State Cir*cuits Conf. (ISSCC) Dig. Tech. Papers, vol. 62, Feb. 2019, pp. 348–350.
- [17] S. Sun, T. Rappaport, R. Heath, A. Nix, and S. Rangan, "MIMO for millimeter-wave wireless communications: Beamforming, spatial multiplexing, or both?" *IEEE Commun. Mag.*, vol. 52, no. 12, pp. 110–121, Dec. 2014.
- [18] A. F. Molisch et al., "Hybrid beamforming for massive MIMO: A survey," IEEE Commun. Mag., vol. 55, no. 9, pp. 134–141, Sep. 2017.
- [19] X. Yu, J.-C. Shen, J. Zhang, and K. B. Letaief, "Alternating minimization algorithms for hybrid precoding in millimeter wave MIMO systems," *IEEE J. Sel. Topics Signal Process.*, vol. 10, no. 3, pp. 485–500, Apr. 2016.
- [20] D. Zhang, Y. Wang, X. Li, and W. Xiang, "Hybridly connected structure for hybrid beamforming in mmWave massive MIMO systems," *IEEE Trans. Commun.*, vol. 66, no. 2, pp. 662–674, Feb. 2018.
- [21] X. Gao, L. Dai, S. Han, C.-L. I, and R. W. Heath, Jr., "Energy-efficient hybrid analog and digital precoding for mmWave MIMO systems with large antenna arrays," *IEEE J. Sel. Areas Commun.*, vol. 34, no. 4, pp. 998–1009, Apr. 2016.
- [22] V. Aparin, G. J. Ballantyne, C. J. Persico, and A. Cicalini, "An integrated LMS adaptive filter of TX leakage for CDMA receiver front ends," *IEEE J. Solid-State Circuits*, vol. 41, no. 5, pp. 1171–1182, May 2006.
- [23] N. Reiskarimian, J. Zhou, and H. Krishnaswamy, "A CMOS passive LPTV nonmagnetic circulator and its application in a full-duplex receiver," *IEEE J. Solid-State Circuits*, vol. 52, no. 5, pp. 1358–1372, May 2017.
- [24] D.-J. van den Broek, E. A. M. Klumperink, and B. Nauta, "A self-interference-cancelling receiver for in-band full-duplex wireless with low distortion under cancellation of strong TX leakage," in *IEEE Int. Solid-State Circuits Conf. (ISSCC) Dig. Tech. Papers*, Feb. 2015, pp. 344–345.
- [25] J. Zhou, T.-H. Chuang, T. Dinc, and H. Krishnaswamy, "Integrated wideband self-interference cancellation in the RF domain for FDD and full-duplex wireless," *IEEE J. Solid-State Circuits*, vol. 50, no. 12, pp. 3015–3031, Dec. 2015.
- [26] T. Dinc, A. Nagulu, and H. Krishnaswamy, "A millimeter-wave non-magnetic passive SOI CMOS circulator based on spatio-temporal conductivity modulation," *IEEE J. Solid-State Circuits*, vol. 52, no. 12, pp. 3276–3292, Dec. 2017.
- [27] A. Nagulu and H. Krishnaswamy, "Non-magnetic 60 GHz SOI CMOS circulator based on loss/dispersion-engineered switched bandpass filters," in *IEEE Int. Solid-State Circuits Conf. (ISSCC) Dig. Tech. Papers*, Feb. 2019, vol. 63, no. 8, pp. 446–448.
- [28] Z. Xiao, P. Xia, and X.-G. Xia, "Full-duplex millimeter-wave communication," *IEEE Wireless Commun.*, vol. 24, no. 6, pp. 136–143, Dec. 2017.
- [29] M. B. Dastjerdi, N. Reiskarimian, T. Chen, G. Zussman, and H. Krishnaswamy, "Full duplex circulator-receiver phased array employing self-interference cancellation via beamforming," in *Proc. IEEE Radio Freq. Integr. Circuits Symp. (RFIC)*, Jun. 2018, pp. 108–111.
- [30] R. Singh, S. Mondal, and J. Paramesh, "A 25.1-27.6 GHz tunable-narrowband digitally-calibrated merged LNA-vector modulator for 5G phased arrays," in *Proc. IEEE Radio Freq. Integr. Circuits Symp. (RFIC)*, Jun. 2018, pp. 4–7.
- [31] S. C. Cripps, Power Amplifiers for Wireless Communication. Norwood, MA, USA: Artech House, 2006.
- [32] X. Li, S. Shekhar, S. Member, and D. J. Allstot, "Gm-boosted commongate LNA and differential colpitts VCO/QVCO in 0.18 μm CMOS," IEEE J. Solid-State Circuits, vol. 40, no. 12, pp. 2609–2619, Dec. 2005.
- [33] P. Haldi, D. Chowdhury, P. Reynaert, G. Liu, and A. M. Niknejad, "A 5.8 GHz 1 v linear power amplifier using a novel on-chip transformer power combiner in standard 90 nm CMOS," *IEEE J. Solid-State Circuits*, vol. 43, no. 5, pp. 1054–1063, May 2008.
- [34] D. Zhao and P. Reynaert, "A 60-GHz dual-mode class AB power amplifier in 40-nm CMOS," *IEEE J. Solid-State Circuits*, vol. 48, no. 10, pp. 2323–2337, Oct. 2013.
- [35] M. Vigilante and P. Reynaert, "A wideband class-AB power amplifier with 29–57-GHz AM–PM compensation in 0.9-V 28-nm bulk CMOS," *IEEE J. Solid-State Circuits*, vol. 53, no. 5, pp. 1288–1301, May 2018.

- [36] N. Deferm and P. Reynaert, "Differential and common mode stability analysis of differential mm-wave CMOS amplifiers with capacitive neutralization," *Anal. Integr. Circuits Signal Process.*, vol. 80, no. 1, pp. 1–12, Jul. 2014.
- [37] V. Bhagavatula, T. Zhang, A. R. Suvarna, and J. C. Rudell, "An ultrawideband IF millimeter-wave receiver with a 20 GHz channel bandwidth using gain-equalized transformers," *IEEE J. Solid-State Circuits*, vol. 51, no. 2, pp. 323–331, Feb. 2016.
- [38] M. Vigilante and P. Reynaert, "On the design of wideband transformer-based fourth order matching networks for E-band receivers in 28-nm CMOS," IEEE J. Solid-State Circuits, vol. 52, no. 8, pp. 2071–2082, Aug. 2017.
- [39] R. Singh, S. Mondal, and J. Paramesh, "A compact digitally-assisted merged LNA vector modulator using coupled resonators for integrated beamforming transceivers," *IEEE Trans. Microw. Theory Techn.*, vol. 67, no. 7, pp. 2555–2568, Jul. 2019.
- [40] M. Spirito, L. C. N. de Vreede, L. K. Nanver, S. Weber, and J. N. Burghartz, "Power amplifier PAE and ruggedness optimization by second-harmonic control," *IEEE J. Solid-State Circuits*, vol. 38, no. 9, pp. 1575–1583, Sep. 2003.
- [41] W. Ye, K. Ma, and K. S. Yeo, "A 2-to-6GHz class-AB power amplifier with 28.4% PAE in 65 nm CMOS supporting 256 QAM," in *IEEE Int. Solid-State Circuits Conf. (ISSCC) Dig. Tech. Papers*, vol. 58, Feb. 2015, pp. 38–39.
- [42] S. Hu, F. Wang, and H. Wang, "A 28 GHz/37 GHz/39 GHz multiband linear Doherty power amplifier for 5G massive MIMO applications," in *IEEE Int. Solid-State Circuits Conf. (ISSCC) Dig. Tech. Papers*, vol. 60, Feb. 2017, pp. 32–33.
- [43] S. Mondal, R. Singh, A. I. Hussein, and J. Paramesh, "A 25–30 GHz 8-antenna 2-stream hybrid beamforming receiver for MIMO communication," in *Proc. IEEE Radio Freq. Integr. Circuits Symp. (RFIC)*, Jun. 2017, pp. 112–115.
- [44] T. Dinc, A. Chakrabarti, and H. Krishnaswamy, "A 60 GHz CMOS full-duplex transceiver and link with polarization-based antenna and RF cancellation," *IEEE J. Solid-State Circuits*, vol. 51, no. 5, pp. 1125–1140, May 2016.
- [45] D.-W. Kang, K.-J. Koh, and G. M. Rebeiz, "A Ku-band two-antenna four-simultaneous beams SiGe BiCMOS phased array receiver," *IEEE Trans. Microw. Theory Techn.*, vol. 58, no. 4, pp. 771–780, Apr. 2010.



Susnata Mondal (Student Member, IEEE) received the B.Tech. and M.Tech. degrees in electronics engineering from IIT Kharagpur, Kharagpur, India, in 2015. He is currently pursuing the Ph.D. degree in electrical and computer engineering with Carnegie Mellon University, Pittsburgh, PA, USA.

In 2013, he was a Research Intern with RWTH Aachen University, Aachen, Germany. From 2014 to 2017, he was a Teaching Assistant with IIT Kharagpur and Carnegie Mellon University. His current research interests include millimeter-wave circuit

and algorithm and system designs for emerging 5G applications.

Mr. Mondal was a recipient of the DAAD WISE Fellowship in 2013, the Best B-Tech Project Award at IIT Kharagpur in 2014, the Analog Devices Outstanding Student Designer Award in 2017, and the IEEE Solid-State Circuits Society Predoctoral Achievement Award in 2019. He was selected as the Solid-State Circuits Society (SSCS) Rising-Star in ISSCC 2020.



Jeyanandh Paramesh (Senior Member, IEEE) received the B.Tech. degree in electrical engineering from IIT Madras, Chennai, India, the M.S. degree in electrical engineering from Oregon State University, Corvallis, OR, USA, and the Ph.D. degree in electrical engineering from the University of Washington, Seattle, WA, USA.

He has held product development and research positions at AKM Semiconductor (Analog Devices), Motorola, and Intel. He is an Adjunct Professor of electrical and computer engineering with Carnegie

Mellon University, Pittsburgh, PA, USA. His current research interests include the design of RF and mixed-signal integrated circuits and systems for a wide variety of applications.